

2022

Information Theoretical Analysis of the Uniqueness of Iris Biometrics

Katelyn M. Hampel
kmhampel@mix.wvu.edu

Follow this and additional works at: <https://researchrepository.wvu.edu/etd>



Part of the [Signal Processing Commons](#)

Recommended Citation

Hampel, Katelyn M., "Information Theoretical Analysis of the Uniqueness of Iris Biometrics" (2022).
Graduate Theses, Dissertations, and Problem Reports. 11218.
<https://researchrepository.wvu.edu/etd/11218>

This Thesis is protected by copyright and/or related rights. It has been brought to you by the The Research Repository @ WVU with permission from the rights-holder(s). You are free to use this Thesis in any way that is permitted by the copyright and related rights legislation that applies to your use. For other uses you must obtain permission from the rights-holder(s) directly, unless additional rights are indicated by a Creative Commons license in the record and/ or on the work itself. This Thesis has been accepted for inclusion in WVU Graduate Theses, Dissertations, and Problem Reports collection by an authorized administrator of The Research Repository @ WVU. For more information, please contact researchrepository@mail.wvu.edu.

Information Theoretical Analysis of the Uniqueness of Iris Biometrics

Katelyn Hampel

Thesis submitted to the
Benjamin M. Statler College of Engineering and Mineral Resources
at West Virginia University
in partial fulfillment of the requirements for the degree of

Master of Science in
Electrical Engineering

Natalia A. Schmid, D.Sc., Chair
Donald Adjero, Ph.D
Brain Woerner, Ph.D

Lane Department of Computer Science and Electrical Engineering

Morgantown, WV
2022

keywords: iris biometrics, IrisCode, population size, iris image
quality, Rate-Distortion, error correction bounds, autoregressive
process, generalized likelihood ratio test

Copyright 2022 Katelyn Hampel

Abstract

Information Theoretical Analysis Of the Uniqueness of Iris Biometrics

Katelyn Hampel

With the rapid globalization of technology in the world, the need for a more reliable and secure online method of authentication is required. This can be achieved by using each individual's distinctive biometric identifiers, such as the face, iris, fingerprint, palmprint, etc.; however, there is a bound to the uniqueness of each identifier and consequently, a limit to the capacity that a biometric recognition system can sustain before false matches occur. Therefore, knowing the limitations on the maximum population that a biometric modality can uniquely represent is essential now more than ever. In an effort to address the general problem, we turn to the use of iris biometrics to measure its uniqueness.

The measure of iris uniqueness was first introduced by John Daugman in 2003 and its analysis since then remained an open research problem. Daugman defines uniqueness as the ability to enroll more and more classes into a recognition system while the probability of collision among the classes remains fixed and near zero. Due to errors while collecting these datasets (such as occlusions, illumination conditions, camera noise, motion, and out-of-focus blur) and quality degradation from any signal processing of the iris data, even the highest in-quality datasets will not approach a perfect zero probability of collision. Because of this, we appeal to techniques presented in information theory to analyze and find the maximum possible population the system can support while also measuring the quality of the iris data present in

the datasets themselves.

The focus of this work is divided into two new techniques to find the maximum population of an iris database: finding the limitations of Daugman’s widely accepted IrisCode and proposing a new methodology leveraging the raw iris data. Firstly, Daugman’s IrisCode is defined as binary templates representing each independent class present in the database. Through the assumption that a one-to-one encoding technique is available to map the IrisCode of each class to a new binary codeword with the length determined by the degrees of freedom inferred from the distribution of distances between each pair of independent class IrisCodes, we can appeal to Rate-Distortion Theory (limits of error-correcting codes) to establish bounds on the maximum population the IrisCode algorithm can sustain using the minimum Hamming distance (HD) between codewords as a quality metric. Our second approach leverages an Autoregressive (AR) model to estimate each iris class’s distinctive power spectral densities and then assume a similar one-to-one mapping of each iris class to a unique Gaussian codeword. A Gaussian Sphere Packing Bound is invoked to realize the maximum population of the dataset and measure the iris quality dependent on the noise present in the data. Another bound, the Daugman-like Bound, is developed that uses the relative entropy between models of classes as a distance metric, like Hamming distance, to find the maximum population given a fixed recognition error for the system. Using these two approaches, we hope to help researchers understand the limitations present in their recognition system depending on the quality of their iris database.

Table of Contents

List of Figures	vii
List of Tables	xiii
1 Introduction	1
1.0 Introduction	1
2.0 Daugman's IrisCode	3
2.0.1 Feature Encoding	3
2.0.2 Recognition	5
2.0.2.1 Pattern Matching	6
2.0.2.2 Measure of Uniqueness/Statistical Independence	9
3.0 Outline of Thesis	14
2 Measuring Iris Uniqueness Given Daugman's IrisCode	15
1.0 Introduction	15
2.0 Development of Bounds	16
2.1 Hamming Bound	17
2.2 Elias-Bassalygo Bound	19
2.3 Plotkin Bound	20
2.4 Gilbert-Varshamov Bound	21

2.5	Findings of Bounds	21
2.6	Actual vs. bound population for $n = 16$	23
3.0	Summary	26
3	Measuring Iris Uniqueness Based on Autoregressive Model	28
1.0	Introduction	28
2.0	Theory, Model, and Analysis	29
2.1	AR model for vectorized iris images	29
2.2	Classical Approach to the Estimation of maximum Population	32
2.3	Log-likelihood Ratio	34
2.4	Asymptotic Case of Log-likelihood Ratio	35
2.5	Analysis of Error Probability, continued	36
2.6	Analysis of iris uniqueness using sphere packing argument . .	37
2.7	A Daugman-like approach to the analysis of iris uniqueness . .	38
3.0	Illustration	40
3.1	Data	40
3.2	Libor Masek Segmentation and Preprocessing Steps	43
3.3	Estimation of Power Spectra	45
3.3.1	Finding Optimal Model Order	46
3.3.2	AR Implementation	56
3.3.3	Justification of ZigZag Iris Unwrapping Methodology	57
3.3.4	Proving Shift-Invariance of AR Model on Estimated Power Spectral Densities	58
3.4	Fitting Relative Frequency Distributions	59
3.5	Sphere Packing Bound	61
3.6	Daugman-like Bound	64

TABLE OF CONTENTS	vi
4.0 Summary	65
4 Proposed Future Work	68
A Related Publications	70

List of Figures

1.1	Encoding scheme of IrisCode using 2D Gabor wavelets. Complex-valued coefficients are generated by projecting a 'patch' of the normalized iris pattern onto quadrature 2D Gabor wavelets. The real and imaginary resulting coefficients create a phasor vector in the complex plane and 1-bit is allocated to both the real and imaginary coordinates. This generates a cyclic or Gray-like code [21], where only one bit changes per quadrature change. Image obtained from [16].	4
1.2	An example of a generated IrisCode shown in upper right-hand corner. This example also shows the results of Daugman's iris localization methodology (not discussed in this thesis). Graphic is extracted from [14].	6
1.3	Histogram plot of Hamming Distances obtained from 9.1 million comparisons between different pairs of irises acquired from iris images from a license database. The solid curve is a resulting binomial probability distribution discussed in the next section, Section 2.0.2.2. Figure obtained from [17].	8
1.4	Biased and skewed histogram of Hamming Distances found from cyclically shifted IrisCodes. The mean-value shifts from $HD = 0.5$, in Figure 1.3, to $HD = 0.458$ due to extreme sampling. Figure obtained from [17].	9

1.5	Figure shows fitted binomial from Figure 1.4 with the found cumulatives, from equation 1.10, for the left-tail Hamming Distances. Figure is obtained from [17].	12
2.1	Illustration of required minimum Hamming Distance, d , between enrollment iris codewords for two classes A and B . The radius r is dependent on the Hamming Distance between the true class codeword (EA/EB) and the query class codeword (QA/QB), denoted by ϵ , and the length of the binary codewords, n . Therefore, $d = 2 \times \lfloor \epsilon \times n \rfloor + 1$, where $r = \lfloor \epsilon \times n \rfloor$, is the needed minimum Hamming Distance between enrolled iris codewords for zero false matches.	18
2.2	Hamming, Elias-Bassalygo, and Plotkin upper bounds and Gilbert-Varshamov lower bound for code length 245 and varying Hamming Distance, ϵ	24
3.1	A block diagram of the proposed methodology.	41
3.2	Example iris images from CASIA (3.2a) and BATH (3.2b). 3.2a shows both upper occlusion, from eyelashes, and lower occlusion, from eyelid. 3.2b shows dominate eyelash occlusion.	42
3.3	Example segmentation and pre-processing steps of a single BATH iris image before ZigZag vectorization is preformed.	44
3.4	An illustration of the ZigZag vectorization of iris images as adapted in this work	45

3.5	Subset of CASIA-IrisV3 Interval dataset that is used to see if texture had an affect on optimal AR model order. Subjects are chosen by varying texture, with Subject 199R having very fine texture to Subject 104L having very rough texture. Only the Real-Valued Gabor Filtered Irises are shown here, due to the high similarities between the real-value and imaginary-value portions of the complex image.	46
3.6	Subset of BATH dataset that is used to see if texture had an affect on optimal AR model order. Subjects are chosen by varying texture, with Subject 13L having very fine texture to Subject 17R having very rough texture. Only the Real-Valued Gabor Filtered Irises are shown here, due to the high similarities between the real-value and imaginary-value portions of the complex image.	47
3.7	Plots of initial average AIC values for a single class for both datasets using original Masek Log-Gabor Filter parameters of $f_0 = 1/18$ and $\sigma = 0.5$. Both plots show the unwanted stair-stepping behavior occurring across all classes average AIC plots.	48
3.8	Reference normalized and cropped iris image for analyzing Gabor filter performance.	48
3.9	Varying center frequencies, f_0 , of CASIA-IrisV3 Interval sample subject 104L. As bandwidth, σ , of Log-Gabor filter is varied, along with center frequency, the normalized iris image's edges become sharper and sharper. Optimal initial center frequency and bandwidth is $f_0 = 1/9$ and $\sigma = 0.5$ by inspection.	50

3.10 Varying center frequencies, f_0 , of BATH sample subject 2R. As bandwidth, σ , of Log-Gabor filter is varied, along with center frequency, the normalized iris image's edges become sharper and sharper. Optimal initial center frequency and bandwidth is $f_0 = 1/9$ and $\sigma = 0.5$ by inspection.	51
3.11 Average AIC plots for CASIA-IrisV3 Interval subject 104L given a center frequency of $f_0 = 1/9$ and varying bandwidths of $\sigma = 0.1$, $\sigma = 0.3$, and $\sigma = 0.5$	52
3.12 Average AIC plots for BATH subject 2R given a center frequency of $f_0 = 1/9$ and varying bandwidths of $\sigma = 0.1$, $\sigma = 0.3$, and $\sigma = 0.5$. . .	52
3.13 Log-Gabor Filtered iris image for subject 104L from CASIA-IrisV3 Interval with varying center frequencies of $f_0 = 1/3$, $f_0 = 1/6$, $f_0 = 1/9$, and $f_0 = 1/12$ and a fixed bandwidth of $\sigma = 0.5$	53
3.14 Log-Gabor Filtered iris image for subject 2R from BATH with varying center frequencies of $f_0 = 1/3$, $f_0 = 1/6$, $f_0 = 1/9$, and $f_0 = 1/12$ and a fixed bandwidth of $\sigma = 0.5$	53
3.15 Average AIC plots for CASIA-IrisV3 Interval subject 104L given a varying center frequency of $f_0 = 1/3$, $f_0 = 1/6$, $f_0 = 1/9$, and $f_0 = 1/12$, with a fixed bandwidth of $\sigma = 0.5$	54
3.16 Average AIC plots for BATH subject 2R given a varying center frequency of $f_0 = 1/3$, $f_0 = 1/6$, $f_0 = 1/9$, and $f_0 = 1/12$, with a fixed bandwidth of $\sigma = 0.5$	54

3.17	Average AIC plots for subset of varying textured irises from CASIA-IrisV3 Interval with fixed Log-Gabor Filter parameters of $f_0 = 1/9$ and $\sigma = 0.5$. Plots demonstrate that varying texture of the iris does not affect the optimal model order of 100. Subject 19L and 53R have the same average AIC plots and overlap (as seen in the figure).	55
3.18	Average AIC plots for subset of varying textured irises from BATH with fixed Log-Gabor Filter parameters of $f_0 = 1/9$ and $\sigma = 0.5$. Plots demonstrate that varying texture of the iris does not affect the optimal model order of 100.	56
3.19	Estimated Power Spectral Densities for both datasets through the use of MATLAB's <i>pburg</i> method.	57
3.20	Row-by-row vectorization.	58
3.21	Estimated power spectral densities of on iris image from the BATH shifted by 1, 10, and 100 pixels compared again the original estimate.	60
3.22	Relative Entropy Imposter distributions for both datasets with best-of-fit chi-square distributions. CASIA-IrisV3 Interval having $K = 4$ degrees of freedom and a fitted variance of $P = 252$, shown in (a), and BATH having $K = 4$ degrees of freedom and a fitted variance of $P = 383$, shown in (b).	61
3.23	Likelihood Imposter distributions for both datasets with best-of-fit chi-square distributions. CASIA-IrisV3 Interval having $K = 4$ degrees of freedom and a fitted variance of $P = 106$, shown in (a), and BATH having $K = 3$ degrees of freedom and a fitted variance of $P = 216$, shown in (b).	62
3.24	Sphere Packing Bound for (a) CASIA-IrisV3 Interval and (b) BATH using the log-likelihood metric.	63

3.25 Sphere Packing Bound for (a) CASIA-IrisV3 Interval and (b) BATH using the relative entropy metric.	64
3.26 Daugman-like Bound for (a) CASIA and (b) BATH datasets.	66

List of Tables

1.1	Cumulatives from Figure 1.5 giving false match probabilities for various HDs. Table extracted from [17].	13
2.1	Hamming (HB), Elias-Bassalygo (EBB), Plotkin (PB), and Gilbert-Varshamov (G-VB) bounds for code length $n = 245$ and varying Hamming Distance, ϵ	25
2.2	Empirically found values of maximal population (Actual) compared against the Hamming (HB), Elias-Bassalygo (EBB), Plotkin (PB), and Gilbert-Varshamov (GVB) bounds for code length $n = 16$	26
3.1	Data reduction performed on CASIA-IrisV3 Interval Database.	43
3.2	Data reduction performed on smaller BATH Database.	43
3.3	Select Sphere Packing Bound Values based on Noise Variance (N) from Figure 3.24 and Figure 3.25.	64
3.4	Subset of Daugman-like bound maximum population values with fixed recognition errors (δ) and varying relative entropy metric (T).	66

Chapter 1

Introduction

1.0 Introduction

New methods involving automated personal identification and verification based on biometrics, such as the face, fingerprint, palmprint, iris, etc., are implemented to improve security [4]. Due to imperfect data collection and intensive post signal processing of the data, biometric recognition systems often perceive characteristics of different human subjects to be similar, as if they belong to the same individual, leading to limits to these recognition systems implemented before false matches occur; because of this, measuring the uniqueness of each biometric is paramount more than ever. We turn to a single biometric to measure uniqueness with this motivation: the iris.

Wildes [38] states that the iris as a biometric modality is the most powerful due to the distinct patterns developed for each individual and its impermeability to change over time. Firstly, the general structure of the iris is created due to genetics, but the subtleties that make each unique are determined randomly during embryonic gestation. This makes the probability of two similar irises extremely low. Secondly, as

a biometric modality iris demonstrates high permanence [2]. Thirdly, unlike fingerprints or face modalities, the iris is protected from external conditions that may harm or affect the iris pattern.

While the iris is regarded as a high performance and high permanence biometric, the capturing of the iris is what produces susceptibility in an iris recognition system. As with any practical data, iris databases are not perfect and experience quality degradation due to occlusions, illumination conditions, camera noise, motion, and out-of-focus blurs (see [33, 8, 28] and references therein). An additional degradation may also follow them due to imperfect signal processing applied while iris images are transformed to meet the required input format to the recognition system. Because of this, the theoretical uniqueness of the iris is affected.

The uniqueness of iris biometrics and methods to evaluate it have been central themes of multiple publications [6, 39, 1, 30]; however, Daugman's approach is perhaps the most accepted methodology proposed thus far. Daugman defines uniqueness as the ability of a recognition system to enroll classes and maintain a near-zero probability of collision between classes. Because of this, the motivation of this thesis is composed of two parts: first, analyzing the limits of Daugman's widely used recognition system through measuring the uniqueness of his IrisCode, and second, developing a new methodology utilizing the raw iris data and transforming data of each iris class to a Gaussian distributed template, with independent and identically distributed Gaussian components. The two models, a binary in the form of IrisCode and a Gaussian extracted from raw iris data, allow the direct application of Channel Coding and Rate-Distortion Theory results from Information Theory [11] to the analysis of iris uniqueness.

2.0 Daugman's IrisCode

Before we can describe our proposed methodologies, the work of Daugman needs to be provided, as this serves as a stepping stone in our work. In [12], Daugman released and patented his well-used algorithm for encoding and recognizing iris patterns that is still used in practice today. Within this algorithm, the ability to localize, segment, normalize, encode, and recognize iris patterns is introduced. For this thesis, we will focus on his implementation of feature encoding and pattern recognition, with a heavy interest in his formulation of the IrisCode.

2.0.1 Feature Encoding

Since the focus of this thesis is centered mainly around the feature encoding techniques and implementation of thresholding presented by Daugman, the localization, and normalization of the iris from an image will not be discussed (see [25] for the Libor Masek's segmentation and normalization for this thesis, which was adopted from Daugman's Rubber Sheet Model [16] and Wildes' mapping algorithm [38]). Because of this, this section will describe Daugman's iris feature encoding using 2D wavelet demodulation assuming that each iris image has been segmented and normalized using his techniques.

Starting with each isolated, normalized, and dimensionless polar iris image, the phase information is extracted through the use of 2D Gabor wavelet filters. In brief, 'patch-wise' regions of the polar iris image are projected onto quadrature 2D Gabor wavelets, generating complex-valued coefficients. These coefficients represent the coordinates of a phasor in the complex plane, where the sign of the real and imaginary coefficients represents two bit values, [1,0]. This encoding process is shown in Figure 1.1, taken from [16].

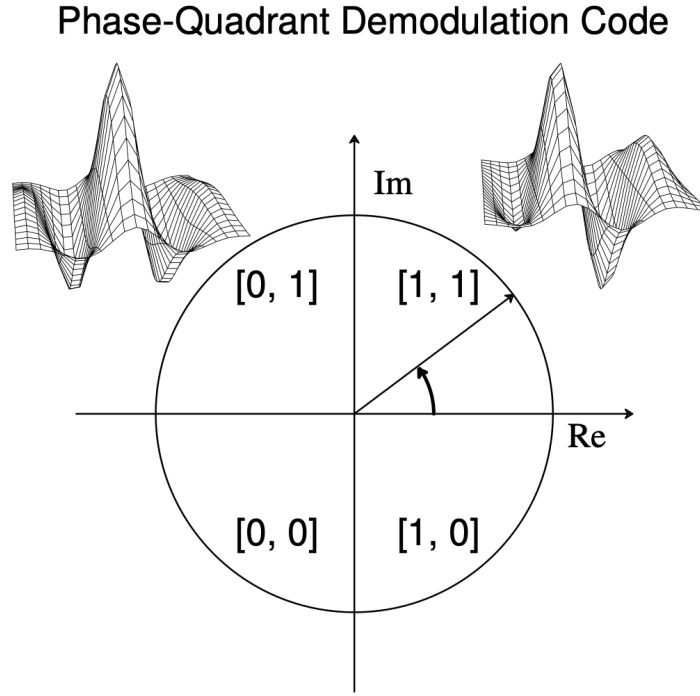


Figure 1.1: Encoding scheme of IrisCode using 2D Gabor wavelets. Complex-valued coefficients are generated by projecting a 'patch' of the normalized iris pattern onto quadrature 2D Gabor wavelets. The real and imaginary resulting coefficients create a phasor vector in the complex plane and 1-bit is allocated to both the real and imaginary coordinates. This generates a cyclic or Gray-like code [21], where only one bit changes per quadrature change. Image obtained from [16].

The encoding procedure, both demodulation and quantization, is described by Daugman in [17] mathematically as

$$h_{Re} = \begin{cases} 1, & \text{if } \text{Re} \int_{\rho} \int_{\phi} e^{-i\omega(\theta_0-\phi)} e^{-(r_0-\rho)^2/\alpha^2} e^{-(\theta_0-\phi)^2/\beta^2} I(\rho, \phi) \rho d\rho d\phi \geq 0, \\ 0, & \text{if } \text{Re} \int_{\rho} \int_{\phi} e^{-i\omega(\theta_0-\phi)} e^{-(r_0-\rho)^2/\alpha^2} e^{-(\theta_0-\phi)^2/\beta^2} I(\rho, \phi) \rho d\rho d\phi < 0; \end{cases} \quad (1.1)$$

and

$$h_{Im} = \begin{cases} 1, & \text{if } \text{Im} \int_{\rho} \int_{\phi} e^{-i\omega(\theta_0-\phi)} e^{-(r_0-\rho)^2/\alpha^2} e^{-(\theta_0-\phi)^2/\beta^2} I(\rho, \phi) \rho d\rho d\phi \geq 0, \\ 0, & \text{if } \text{Im} \int_{\rho} \int_{\phi} e^{-i\omega(\theta_0-\phi)} e^{-(r_0-\rho)^2/\alpha^2} e^{-(\theta_0-\phi)^2/\beta^2} I(\rho, \phi) \rho d\rho d\phi < 0. \end{cases} \quad (1.2)$$

From equations 1.1 and 1.2 above, $I(\rho, \phi)$ is the raw dimensionless phasor iris image, where (ρ, ϕ) are the polar coordinates of each region of the iris; α and β are the 2D wavelet scale parameters; and ω is the wavelet frequency (inversely proportional of β). The IrisCode, h , is then composed of two bits for each iris region, where $h = h_{Re} + h_{Im}$. Because of the quadrature encoding, the bit behaves similar to cyclic or Gray code [21], as only one bit changes between adjacent quadrants. This coding scheme increases the reliability of the code, as only a single code bit can change (verses two bits using a binary encoding scheme).

After the pair of code bits are found for each local iris region, the IrisCode is composed of 2048 bits (256 bytes). Daugman also creates an equal number of masking bits jointly to account for occlusions, boundary artifacts, and poor signal-to-noise ratio to be used later for recognition. As equations 1.1 and 1.2 show, only the phase information of the iris is considered when generating the IrisCode. In [17], Daugman claims that the amplitude is not very discriminating and is highly sensitive to imaging conditions, such as illumination, contrast, and camera gain. He also proves that when only looking at phase information, the IrisCode is very robust against out-of-focus iris images, and the code generated is very similar to the same properly focused iris. Figure 1.2 shows an IrisCode generated by Daugman.

2.0.2 Recognition

Now that we have obtained a unique IrisCode to represent each iris class, Daugman's methodology to pattern matching can be introduced, along with his measure for statistical independence (uniqueness) between iris classes. Section 2.0.2.1 summarizes Daugman's approach to matching two IrisCodes through the use of Hamming Distances. Section 2.0.2.2 briefly describes how he quantifies uniqueness in IrisCode through the use of measuring statistical independence between IrisCodes.

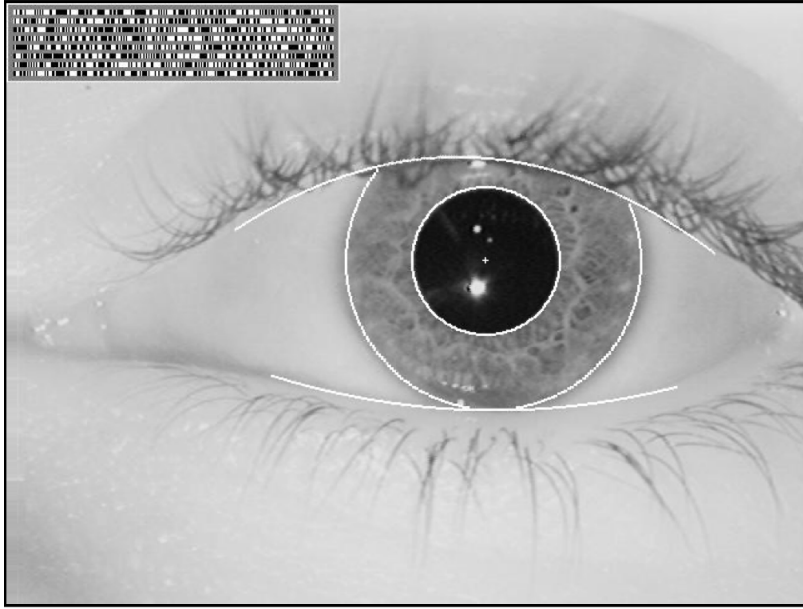


Figure 1.2: An example of a generated IrisCode shown in upper right-hand corner. This example also shows the results of Daugman’s iris localization methodology (not discussed in this thesis). Graphic is extracted from [14].

2.0.2.1 Pattern Matching To compare two IrisCodes, Daugman first introduces Hamming Distance (HD) in [17] to measure the bit-wise differences between two classes. The HD used by Daugman is described mathematically as

$$HD = \frac{1}{N} \sum_{k=1}^N X_k \otimes Y_k, \quad (1.3)$$

where an Exclusive OR (\otimes) detects the disagreement between the two binary vectors X and Y , each of length N . A perfect match between two IrisCodes of length 2048 bits, would result in a $HD = 0$, as there are no bit changes between each binary vector/codeword.

To accommodate for occlusions, such as eyelashes, eyelids, reflections, or other noise, Daugman modifies equation 1.3 to include the binary masks generated at the same time as the IrisCodes to account for such distortions/artifacts. To measure the distance between two IrisCodes (given as $\{\text{codeA}, \text{codeB}\}$) without considering

these artifacts, each classes' IrisCode is XOR'ed (\otimes) to find dissimilarities, then the corresponding mask binary vectors ($\{\text{maskA}, \text{maskB}\}$) are AND'ed (\cap) with this resulting binary vector to prevent occlusions being involved in iris comparisons. This is described mathematically as follows

$$HD = \frac{\|(\text{codeA} \otimes \text{codeB}) \cap \text{maskA} \cap \text{maskB}\|}{\|\text{maskA} \cap \text{maskB}\|}. \quad (1.4)$$

The denominator represents the total number of bits that mattered in iris comparison; therefore, the resulting HD is a fractional HD of the entire IrisCode (as all 2048 bits may not contain pure iris patterns). The norm ($\| \ \|$) of both the numerator and denominator are taken in equation 1.4 to measure the dissimilarity between the two iris classes and give the resulting fractional HD.

Because the difference between phase bits in the IrisCodes of two different individuals has an equal probability of being a 1 or 0, the HD distribution is centered around $HD = 0.5$. Daugman proves this in [17] by plotting the relative frequencies of the imposter HDs, shown in Figure 1.3, and the lowest HD observed was $HD = 0.334$. The fitted binomial in this figure will be discussed in the next section, Section 2.0.2.2.

Presented in [17] is the ability of the IrisCode to be invariant to the following: iris orientation, caused by head-tilt or camera tilt/angles during acquisition; location and size of the iris within the image, dependent on the distance between camera and subject; and the size of the pupil within the iris (as this affects the size of the iris, compresses or expands the iris depending on dilation of the pupil). Daugman addresses the location and size of the iris/pupil with his rubber sheet model, as this provides a solid mapping from the Cartesian iris image $I(x, y)$ to the dimensionless polar coordinate system $I(r, \theta)$. For the concern of this thesis, we are focused on the orientation of the iris image within the image plane.

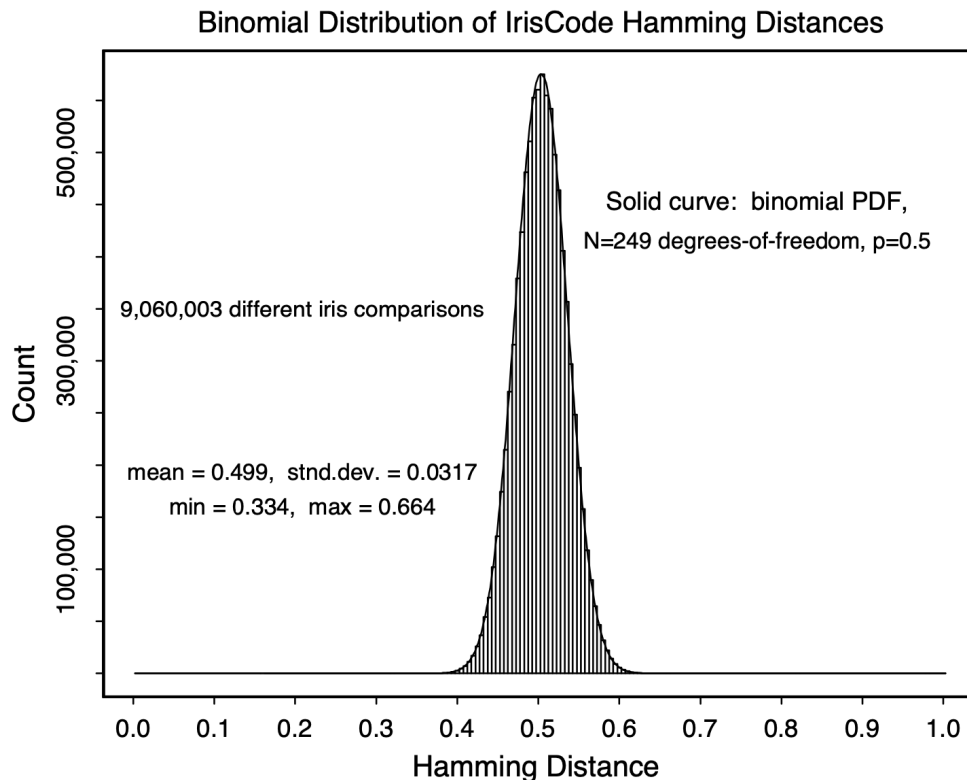


Figure 1.3: Histogram plot of Hamming Distances obtained from 9.1 million comparisons between different pairs of irises acquired from iris images from a license database. The solid curve is a resulting binomial probability distribution discussed in the next section, Section 2.0.2.2. Figure obtained from [17].

To address this, Daugman cyclically scrolls one of the IrisCodes with respect to the other IrisCode, as scrolling in the polar domain is the same as rotation in the Cartesian plane. Matching is performed between two IrisCodes multiple times while shifting one IrisCode by k bits up to ± 7 bits. The smallest HD is retained from the matched rotations. The resulting histogram is skewed and biased to a lower mean ($HD = 0.458$), which is due to the extreme sampling during the experiment. Although this histogram is not centered at $HD = 0.5$, the lowest HD obtained is 0.33 and shows that less than a third of the skewed IrisCodes disagree (the same results presented for the non-skewed IrisCode imposter distribution). These results prove

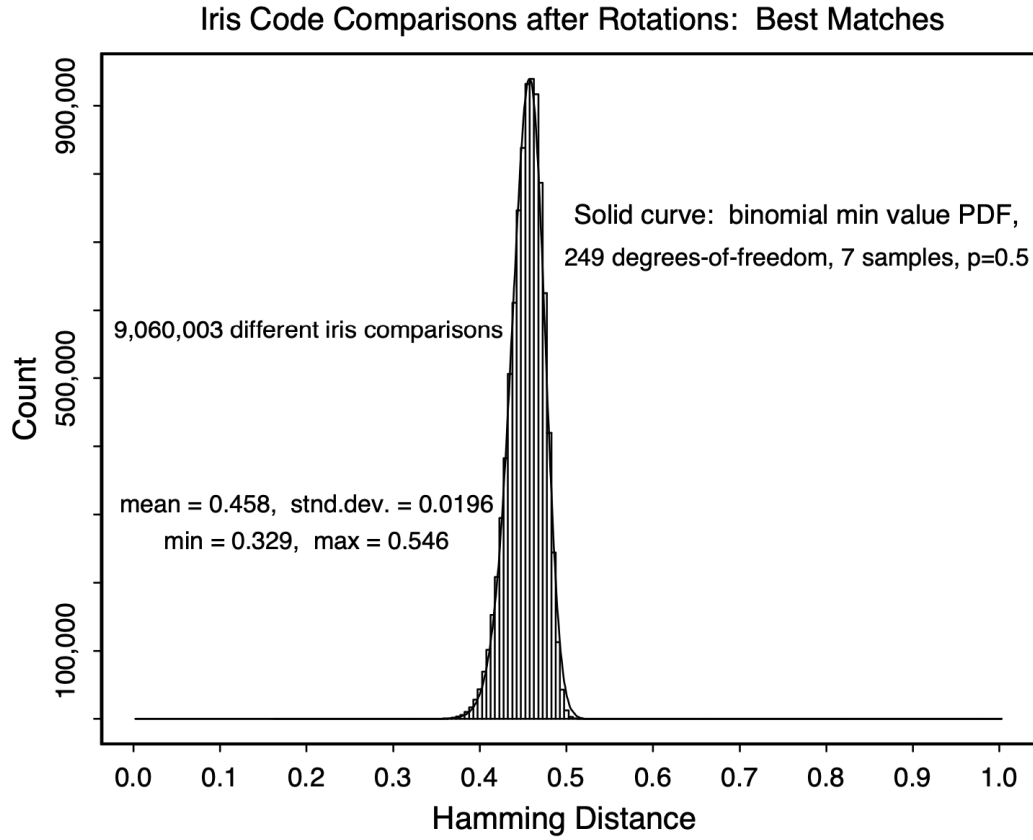


Figure 1.4: Biased and skewed histogram of Hamming Distances found from cyclically shifted IrisCodes. The mean-value shifts from $HD = 0.5$, in Figure 1.3, to $HD = 0.458$ due to extreme sampling. Figure obtained from [17].

that the IrisCode is rotationally invariant and can compensate for acquisition errors, which prove detrimental to many recognition systems and do not affect the deciding threshold for his proposed recognition discussed in Section 2.0.2.2. Figure 1.4 shows the results discussed above.

2.0.2.2 Measure of Uniqueness/Statistical Independence In [14, 16, 17], Daugman proposed measuring uniqueness of the iris through the use of analyzing the distribution of imposter match scores, shown in Figure 1.3. From this figure, we can see that the observed mean of the Hamming Distance relative frequencies is

$mean = 0.499$ with a standard deviation of $\sigma = 0.0317$. Due to the shape of this distribution, it can be fitted closely with a fractional binomial probability density function (pdf) given as

$$f(x) = \sum_{m=0}^N \frac{N!}{m!(N-m)!} p^m (1-p)^{(N-m)} \delta(x-m), \quad (1.5)$$

where $N = p(1-p)/\sigma^2 = 249$, $p = 0.5$, x is the HD (fraction of IrisCode bits between two different iris classes that disagree during comparison), and $\delta(\cdot)$ is the Dirac delta function. The fitted distribution is shown in Figure 1.3 by the solid curve.

The shape of this tightly fitted pdf describes the amount of difference between pairwise matchings of different IrisCodes. It can be represented through N independent Bernoulli Trials (with $N = 249$ and $p = 0.5$). From this observation, Daugman then extrapolates a discrimination entropy by concluding that each iris contains N bits of information (or $N = 249$ bits of information).

To formulate his discrimination entropy, Daugman assumes typical iris and pupil diameters of $r_{iris} = 11mm$ and $r_{pupil} = 5mm$. The information measure is found through dividing the N degrees-of-freedom by the area of the iris and is shown in [12] as

$$\frac{N}{\text{iris area}} = \frac{N}{\pi r_{iris}^2 - \pi r_{pupil}^2} \approx 3.2 \text{bits/mm}^2. \quad (1.6)$$

This measure of informational density describes the variability among different iris patterns, in that the likelihood of another iris containing the same information as a portion of the comparative iris is equivalent to N Bernoulli Trials.

For this thesis, we will not focus on his measure of discrimination entropy to measure iris uniqueness and instead look at how Daugman derived a threshold based

on this new fitted fractional binomial distribution. From [17], assume that $f_0(x)$ is computed similar to the binomial pdf in Figure 1.3. The cumulative of $f_0(x)$, $F_0(x)$, is a probability of getting a false match when the acceptance threshold is x :

$$F_0(x) = \int_0^x f_0(x)dx \quad (1.7)$$

or

$$f_0(x) = \frac{d}{dx}F_0(x). \quad (1.8)$$

Then, looking at the left-hand tail, the probability of not making a false match after a single test is $1 - F_0(x)$, and equivalently after n tests, measuring different orientations of the IrisCode similar to Figure 1.4, is $[1 - F_0(x)]^n$. Thus, the probability of a false match after n tests using the threshold x is

$$F_n(x) = 1 - [1 - F_0(x)]^n. \quad (1.9)$$

The equivalent probability density $f_n(x)$ is given as

$$f_n(x) = \frac{d}{dx}F_n(x) = nf_0(x)[1 - F_0(x)]^{n-1}. \quad (1.10)$$

Figure 1.5 shows the binomial probability distribution given in Figure 1.4 with the found cumulatives from equation 1.10. Here we can see that a $HD \leq 0.32$, or that two IrisCodes disagree, is extremely improbable, about 1 in 26 million. Therefore, in order to recognize IrisCodes from the same class (genuines) with zero collisions/high confidence, a loose threshold of $HD \leq 0.32$ is set. Table 1.1 gives the probabilities of a false match given a specific HD, extracted from Figure 1.5.

Finally, Daugman analyzes how the population of an iris database affects total

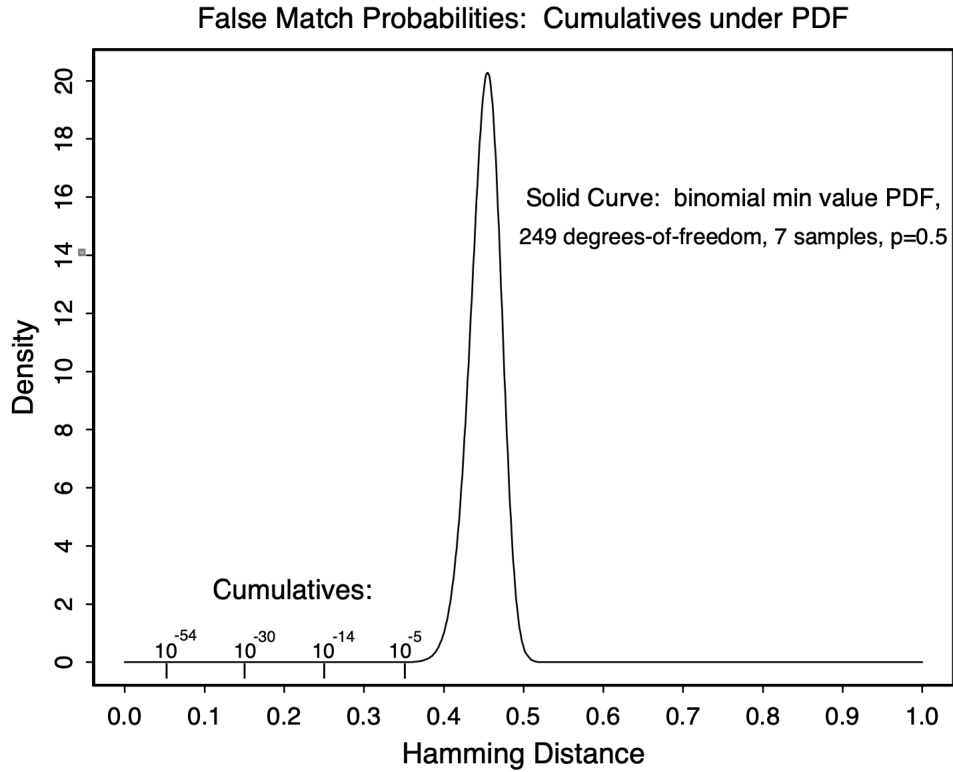


Figure 1.5: Figure shows fitted binomial from Figure 1.4 with the found cumulatives, from equation 1.10, for the left-tail Hamming Distances. Figure is obtained from [17].

recognition error in a verification scenario (one-to-many), based off of the false match rates for one-to-one matching (demonstrated above in Table 1.1). The probability of making at least one false match, P_N , while searching a database of N classes is given as

$$P_N = 1 - (1 - P_1)^N, \quad (1.11)$$

where P_1 is the probability of making a false match in single comparisons.

In [17], he analyzes the effects that the population, N , has on the total recognition error, P_N . Because of this, Daugman concludes that when searching a database of size N (identification scenario), the search threshold, HD, needs to be adaptive given a fixed desired recognition error. For example, if a search database contains 1 million

Table 1.1: Cumulatives from Figure 1.5 giving false match probabilities for various HDs. Table extracted from [17].

HD criterion	Odds of false match
0.26	1 in 10^{13}
0.27	1 in 10^{12}
0.28	1 in 10^{11}
0.29	1 in 13 billion
0.30	1 in 1.5 billion
0.31	1 in 185 million
0.32	1 in 26 million
0.33	1 in 4 million
0.34	1 in 690,000
0.35	1 in 133,000
0.36	1 in 28,000
0.37	1 in 6750
0.38	1 in 1780
0.39	1 in 520
0.40	1 in 170

iris classes, then in order to maintain a recognition error, let us say $P_N < 10^{-6}$, then the threshold/HD will need to be adjusted downwards from 0.32 to 0.27.

3.0 Outline of Thesis

Building upon Daugman's methodology presented above, this thesis consists of four chapters. Chapter 2 leverages the use of Rate-Distortion theory through the use of error-correcting bounds on a binary codeword. Here we assume a one-to-one mapping from Daugman's IrisCode to a binary codeword is available, and present upper bounds, along with a lower bound, to characterise the uniqueness of IrisCode in terms of the maximal population that the IrisCode algorithm can sustain given that iris data are constrained to have a specific level of quality. In Chapter 3, we present a new methodology to measure uniqueness by assuming a Gaussian model for each unwrapped and vectorized iris image and then finding the unique estimated power spectral density of each iris class through the use of an Autoregressive model. We then presume that a mapping is available to map each class iris data to a unique Gaussian codeword, based off of the fitted degrees of freedom of each databases' distance metrics relative frequencies. Given these assumptions, the uniqueness of iris biometrics for this case can be analysed using the Channel Coding Theorem for Gaussian models, a well established result from Information Theory. Finally, Chapter 4 describes possible directions the form of this work can take.

Chapter 2

Measuring Iris Uniqueness Given Daugman's IrisCode

1.0 Introduction

This chapter focuses on understanding the performance limits of Daugman's iris recognition system using the IrisCode (see [12, 17, 14, 16, 15]). From his previous work, discussed in the above Section 2.0, he proposed that an individual iris's information can be represented by 249 (or 245 in [15]) bits based on the fitted degrees of freedom of a fractional binomial. In combination with this, he also analyzed that while one-to-one (or verification) matching performance is excellent using the IrisCode; however, when it comes to one-to-many (or identification) performance, the size of the iris dataset widely affects the recognition error given a fixed/desired false match rate based on Hamming Distances. Because he gives an estimate of the maximum population his dataset can obtain based on the imposter distributions (see equation 1.11), the analysis of image quality is not discussed, nor are the effects it has on choosing a proper Hamming distance threshold. Because of this, we turn to

Rate-Distortion theory Sphere-Packing Bounds on error-correcting codes to find the upper and lower limits to Daugman's IrisCode while also analyzing image quality.

In Section 2.0, we present the development of a new Hamming distance, d , such that there are no overlaps between the iris classes. Using this new distance, the Hamming, Elias-Bassalygo, and Plotkin upper bounds are derived, along with the Gilbert-Varshamov lower bound. We discuss the limits of Daugman's IrisCode in Section 2.5, while also giving an example of the actual maximum population achievable with zero collision and the bounds given population using a smaller codeword length, $n = 16$. Finally, a summary of the performance of these bounds is given in Section 3.0.

2.0 Development of Bounds

The following derivation assumes a one-to-one mapping available from Daugman's IrisCode of 2048 bits to a binary codeword of length $n = 245$ for each iris class. This codeword length is dependent on the imposter binomial's fitted degrees of freedom, shown in Figure 1.3 (however, for this work, we use the latest fitted binomial from [15] that uses $n = 245$ degrees-of-freedom). Now that we have a unique binary codeword to represent each iris class present in the system, we can turn to Rate-Distortion Theory [11] (or, more specifically, bounds on error-correcting codes) to find the limitations of Daugman's algorithm given a fixed Hamming distance (HD) between two codewords using sphere-packing bounds.

To begin, let us create an idealized space. Assume that all enrolled iris classes' codeword acts as a 'ground truth' for each iris class and can be represented by a point in 2^n codespace on an n -dimensional lattice. For illustrative purposes and understanding, let us consider that only two iris classes are enrolled in the recognition

system, Class A and Class B . Next, let us consider a query iris codeword is submitted to the recognition system and is also represented as a point; let us say this query codeword belongs to Class A , and the HD between the actual iris codeword and the query codeword is denoted as ϵ and represents the distortions and noise present in the query codeword (distance between genuine classes). With this relationship, we can now claim that the actual codeword and query codeword lie within a hyper-dimensional sphere of radius r , where r and ϵ are related as

$$r = \lfloor \epsilon \times n \rfloor, \text{ bits.}$$

Now, let us add a query iris codeword that belongs to Class B into the system for recognition. This query codeword will now lie within the hyper-dimensional sphere of radius r for Class B . Given these two spheres, we can show in Figure 2.1 that for two iris classes to be distinguishable while matching, the spheres cannot overlap, as this would introduce false matches. Because of this, the centers of both classes' hyper-dimensional spheres have to be spaced at least $r \times 2 + 1 = \lfloor \epsilon \times n \rfloor \times 2 + 1 = d$ bits apart, where d is the new required HD between two hyper-dimensional spheres. Applying this simple thought experiment to an entire recognition system, we can apply the following upper bounds and lower bounds from Rate-Distortion Theory to obtain a confidence band on the maximum population Daugman's IrisCode can support given our new minimum HD d .

2.1 Hamming Bound

To begin our theoretical analysis of the maximum population of Daugman's IrisCode, along with our newly derived minimum Hamming Distance d , we turn to the loose upper bound on error-correcting codes: the Hamming Bound. From [24, 29, 34], the

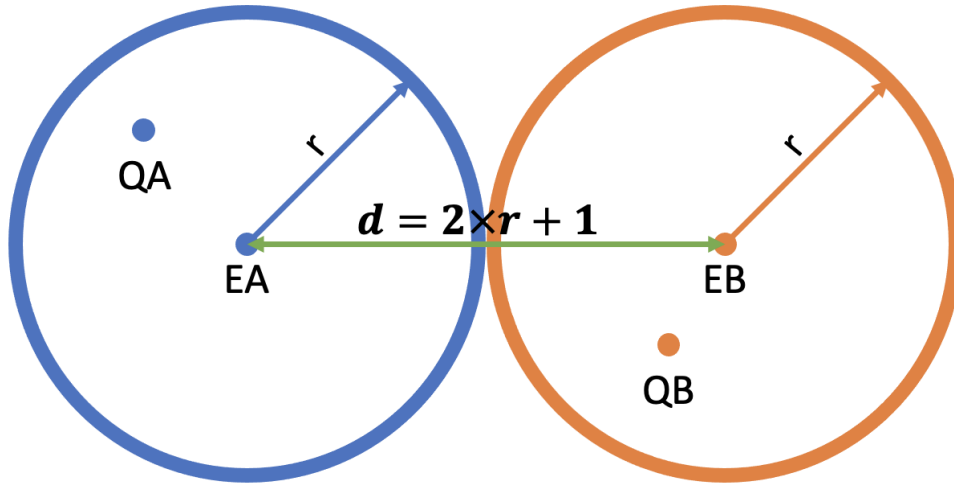


Figure 2.1: Illustration of required minimum Hamming Distance, d , between enrollment iris codewords for two classes A and B . The radius r is dependent on the Hamming Distance between the true class codeword (EA/EB) and the query class codeword (QA/QB), denoted by ϵ , and the length of the binary codewords, n . Therefore, $d = 2 \times \lfloor \epsilon \times n \rfloor + 1$, where $r = \lfloor \epsilon \times n \rfloor$, is the needed minimum Hamming Distance between enrolled iris codewords for zero false matches.

Hamming bound is as follows

$$A(n, r) \leq \frac{2^n}{\sum_{i=0}^r \binom{n}{i}}, \quad (2.1)$$

where $A(n, r)$ is the maximum population dependent on n , which is the length of the iris codeword, and the radius of the sphere, $r = \lfloor \epsilon \times n \rfloor$, bits. In Section 2.5, we will look at the resulting upper bound values on the maximum population for the IrisCode.

2.2 Elias-Bassalygo Bound

Since the Hamming Bound above is a loose upper bound for all Hamming Distances, we provide a tighter upper bound for lower values of Hamming Distance: the Elias-Bassalygo Bound. In the original publication [5], Bassalygo formulates the bound given the condition $1 \leq d \leq n/2$ as

$$A(n, d) \leq \left\lfloor \frac{n 2^{n+1}}{\binom{n}{J(n, d)}} \right\rfloor, \quad (2.2)$$

where $J(n, r)$ is the following Johnson Bound

$$J(n, d) = \left\lfloor \frac{n - \sqrt{n(n - 2d)}}{2} \right\rfloor.$$

Given our new found minimum Hamming Distance, d from above, we can reformulate equation 2.2 in relation to the radius r of the hyper-dimensional spheres describing each iris class without overlap. Substituting $d = 2 \times r + 1$ into equation 2.2, the following Elias-Bassalygo upper bound, given the constraint $r \leq (n-2)/4$, is described as

$$A(n, r) \leq \left\lfloor \frac{n 2^{n+1}}{\binom{n}{J(n, r)}} \right\rfloor, \quad (2.3)$$

where $J(n, r)$ is the following

$$J(n, r) = \left\lfloor \frac{n}{2} \left(1 - \sqrt{1 - \frac{2(2r + 1)}{n}} \right) \right\rfloor.$$

2.3 Plotkin Bound

Another tighter upper bound on the maximum population of the IrisCode implemented is the Plotkin Bound. The Plotkin bound compensates for the higher Hamming Distances in which the Elias-Bassalygo bound is not applicable. From [27], the bound takes these several forms

1. If d is even and $2d > n$, then

$$A(n, d) \leq 2 \left\lfloor \frac{d}{2d - n} \right\rfloor. \quad (2.4)$$

2. If d is odd and $2d + 1 > n$, then

$$A(n, d) \leq 2 \left\lfloor \frac{d + 1}{2d + 1 - n} \right\rfloor. \quad (2.5)$$

3. If d is even and $2d = n$, then

$$A(2d, d) \leq 4d. \quad (2.6)$$

4. If d is odd and $2d + 1 = n$, then

$$A(2d + 1, d) \leq 4d + 4. \quad (2.7)$$

Since $d = 2 \times r + 1$ is always an odd number, we only look at the bounds presented in equations 2.5 and 2.7 and can be reformulated substituting our values for d . Given $r \geq (n - 3)/4$, the Plotkin Bound on maximum population given in equation 2.5 is

$$A(n, r) \leq 2 \left\lfloor \frac{2r + 2}{4r + 3 - n} \right\rfloor. \quad (2.8)$$

Similarly, if $4r + 3 = n$, then equation 2.7 can be rewritten in terms of r as

$$A(n, r) = A(4r + 3, r) \leq 8r + 8. \quad (2.9)$$

2.4 Gilbert-Varshamov Bound

The last bound implemented to find the maximum population attainable by Daugman's IrisCode is the tight lower bound called the Gilbert-Varshamov Bound. From [19, 24, 36], the Gilbert-Varshamov Bound is constructed by assuming that all codeword hyper-dimensional spheres are present and overlapping in a 2^n codespace. From this, a class is selected at random and any neighboring classes that are of distance $d - 1$ or less are removed from the space. From the remaining classes, this process is repeated until no more neighboring spheres overlap (all greater than a distance of $d - 1$). The remaining set of classes ensures that each classes' codeword will have a minimum distance d . The bound is described mathematically as

$$A(n, r) \geq \left\lceil \frac{2^n}{\sum_{i=0}^{2r} \binom{n}{i}} \right\rceil. \quad (2.10)$$

2.5 Findings of Bounds

This section discusses our findings of the Hamming, Elias-Bassalygo, Plotkin, and Gilbert-Varshamov Bounds derived in Section 2.0. In Daugman's work, he chooses the optimal Hamming Distance that is sustainable in an iris database from the threshold (ϵ) of the imposter distribution, shown in Figure 1.3 from Section 2.0, to evaluate the maximum population his recognition system can sustain. Looking at favorable conditions only, where the same camera, distance, lighting, and setup were used [17], the optimal threshold is chosen where there is a guarantee of no collisions between

IrisCodes from the imposter distribution at $\epsilon = 0.32$. For the analysis of IrisCodes, we look at a range of Hamming Distance thresholds, from $\epsilon = 0.12$ to $\epsilon = 0.36$, and a codeword length of $n = 245$ for all bounds. A graphical representation of the bounds is shown in Figure 2.2. A subset of ϵ values are extracted from Figure 2.2 and is shown in Table 2.1 for the upper and lower bounds.

Firstly, looking at Figure 2.2, there is a clear disconnect between the Elias-Bassalygo and Plotkin Bounds. This is due to the constraint on each bound from equations 2.2 and 2.5. Let us first look at the Elias-Bassalygo bound; here, the bound is only applicable where $r \leq (n - 2)/4$. If $n = 245$, then the Elias-Bassalygo bound can be applied for $r \leq 60.75$ (or $\epsilon \approx 0.25$ bits). The Plotkin bound bridges this gap with a constraint of $r \geq (n - 3)/4 = 60.5$ (or $\epsilon \approx 0.25$ bits). From the figure, the Elias-Bassalygo bound gives a tighter upper bound constraint on the maximum achievable population supported by Daugman's IrisCode then compared to the Hamming bound, for threshold values $\epsilon \leq 0.25$. The Plotkin bound also gives a tighter maximum population for thresholds $\epsilon \geq 0.25$ compared to the Hamming bound; however, the bound eventually converges with the Gilbert-Varshamov bound at $\epsilon \approx 0.34$, as seen in Table 2.1.

From Table 2.1, it is clear that the IrisCode cannot enroll many iris classes when the threshold ϵ is set at or above 0.28, let alone at Daugman's threshold of 0.32. Decreasing this threshold increases the maximum population considerably. If a new threshold range of $\epsilon = 0.2$ to $\epsilon = 0.12$ is chosen, then the recognition system, according to the Elias-Bassalygo bound, can support a maximum population of 3.82×10^{21} and 1.26×10^{36} classes with zero collisions between the enrolled classes. While the Hamming bound gives a large maximum population, the more realistic and attainable populations are given by the Elias-Bassalygo bound with a maximum population of 6.98×10^{14} and 5.30×10^{34} , respectively. Concomitantly, the Gilbert-Varshamov lower

bound gives the minimum, maximum population sustainable as 952 and 3.84×10^{16} . These larger maximum populations are dependent only if the query and enrollment data submitted into the recognition system are of the same extremely high-quality.

Although a threshold of $\epsilon \leq 0.20$ seems challenging, this new lower threshold is achievable due to advancements in technology. State-of-the-art image acquisition cameras (including those in our cell phones) take multi-view video sequences of an object and then interpolate them in a single view capture of the highest possible quality. In addition, given a video of an iris, various signal processing, and machine learning approaches can be applied to ensure high quality of IrisCode templates [40]. As the quality of the enrollment and query iris images submitted to the system is increased, the imposter distribution becomes more centered around $HD = 0.5$ (standard deviation decreases), and a lower threshold is obtained as the false match probability (the cumulative in the right tail of the imposter distribution) becomes increasingly tiny and improbable. By finding the maximum population achievable by the system given these bounds, we also measure the quality of the iris images present within the system (both enrollment and query data). In conclusion, the maximum population of the system is directly dependent on the quality of the iris images.

2.6 Actual vs. bound population for $n = 16$

To solidify the trends present in the theoretical bounds for maximum population, we perform an exhaustive search on all binary codewords of length $n = 16$ to find the empirical maximum population. This smaller codeword length is chosen due to the computational complexity and time required to run an extensive search on all possible codewords of length $n = 245$ in a codespace of 2^{245} . The remainder of this section demonstrates that the maximum population of the IrisCode will fall between

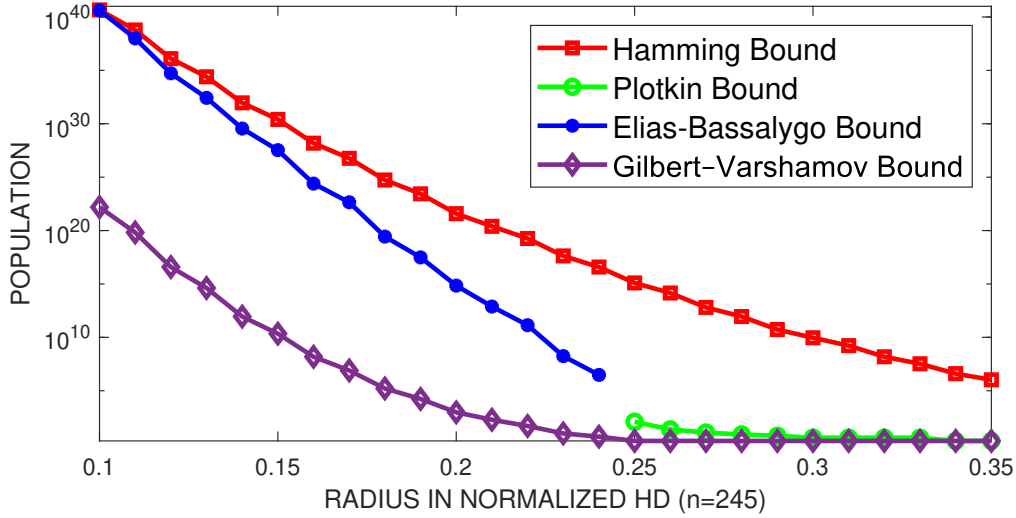


Figure 2.2: Hamming, Elias-Bassalygo, and Plotkin upper bounds and Gilbert-Varshamov lower bound for code length 245 and varying Hamming Distance, ϵ .

the upper and lower bounds presented above.

To begin, an exhaustive search algorithm was implemented where all codewords of length $n = 16$ were generated using MATLAB. Like the development of the Gilbert-Varshamov bound, a single codeword is chosen from the codespace, and the neighboring codewords that are equal to or lie below the threshold ϵ are removed from the space. This continues until all codewords are spaced by a distance of $\lfloor \epsilon \times n \rfloor \times 2 + 1$ apart, ensuring no collisions. The actual maximum population is given in Table 2.2 along with the Hamming, Elias-Bassalygo, Plotkin upper bounds, and the Gilbert-Varshamov lower bound for codewords of length $n = 16$.

Table 2.2 demonstrates that when the threshold is larger, $\epsilon = 0.26$ to $\epsilon = 0.36$, the theoretical population converges to the actual population found. For the smaller threshold values, $\epsilon = 0.22$ to $\epsilon = 0.12$, the theoretical population closest to the actual population is given by the Hamming bound of 94 to 3855 classes, respectively. While these results are somewhat contradictory to our upper theoretical trends presented

Table 2.1: Hamming (HB), Elias-Bassalygo (EBB), Plotkin (PB), and Gilbert-Varshamov (G-VB) bounds for code length $n = 245$ and varying Hamming Distance, ϵ .

ϵ	r , bits	d , bits	HB	EBB	PB	GVB
0.12	29	59	1.26×10^{36}	5.30×10^{34}	N/A	3.84×10^{16}
0.14	34	69	9.09×10^{31}	3.57×10^{29}	N/A	8.87×10^{11}
0.16	39	79	1.52×10^{28}	2.48×10^{24}	N/A	1.52×10^8
0.18	44	89	5.42×10^{24}	2.71×10^{19}	N/A	1.62×10^5
0.20	49	99	3.82×10^{21}	6.98×10^{14}	N/A	952
0.22	53	107	1.81×10^{19}	1.37×10^{11}	N/A	50
0.24	58	117	3.84×10^{16}	3.04×10^6	N/A	5
0.26	63	127	1.42×10^{14}	N/A	24	2
0.28	68	137	8.87×10^{11}	N/A	8	2
0.30	73	147	9.14×10^9	N/A	4	2
0.32	78	157	1.52×10^8	N/A	4	2
0.34	83	167	3.98×10^6	N/A	2	2
0.36	88	177	1.62×10^5	N/A	2	2

in Figure 2.2, this is due to the small codeword length affecting the Elias-Bassalygo bound. The performance of the Elias-Bassalygo bound increases as n is increased asymptotically. Looking at the lower Gilbert-Varshamov bound, the values provided are quite low and loose.

In closing, the bounds given for the smaller codeword length, $n = 16$, prove that our actual achievable population is constrained by the upper Hamming and the lower Gilbert-Varshamov bounds. Although the Elias-Bassalygo bound did not produce excellent results, this is due to the minimal codeword length chosen n . As n increases, the bound will asymptotically become tighter to the maximum realizable population. This small demonstration also validates that for $\epsilon \geq 0.26$, the IrisCode cannot sustain a large population and that if the threshold ϵ is shifted to the right, then larger maximum populations are obtainable.

Table 2.2: Empirically found values of maximal population (Actual) compared against the Hamming (HB), Elias-Bassalygo (EBB), Plotkin (PB), and Gilbert-Varshamov (GVB) bounds for code length $n = 16$.

ϵ	d , bits	HB	EBB	PB	Actual	GVB
0.12	3	3855	131072	N/A	2048	479
0.14	5	478	3744	N/A	256	27
0.16	5	478	3744	N/A	256	27
0.18	5	478	3744	N/A	256	27
0.20	7	94	480	N/A	32	5
0.22	7	94	480	N/A	32	5
0.24	7	94	480	N/A	32	5
0.26	9	26	N/A	6	4	2
0.28	9	26	N/A	6	4	2
0.30	9	26	N/A	6	4	2
0.32	11	9	N/A	2	2	2
0.34	11	9	N/A	2	2	2
0.36	11	9	N/A	2	2	2

3.0 Summary

This chapter introduces the application of Rate-Distortion Sphere-Packing bounds to find the maximum population of an iris recognition system given Daugman's IrisCode. Given that there exists a one-to-one mapping for each iris class into a binary codeword of length $n = 245$, each class and its tolerable variations (noise) can be represented by a hyper-dimensional sphere in 2^{245} space. From Section 2.0, a new minimum normalized Hamming Distance d between each iris classes' hyper-dimensional spheres was developed dependent on the threshold ϵ of the imposter Hamming distance distribution for the entire system and the length of the codeword n . The sphere-packing bounds presented in Rate-Distortion Theory are derived using the new HD d to find the maximum population sustainable by the system while ensuring no collisions between classes occur.

The findings presented in Section 2.5 show that the Hamming bound provides a loose upper limit on the maximum population, while the combination of the Elias-Bassalygo and Plotkin bounds provide a tighter fit for all threshold, ϵ , distances. The Gilbert-Varshamov lower bound gives insight into what the lowest maximum population is achievable. Daugman's optimal threshold of $\epsilon = 0.32$ shows that his proposed recognition system cannot handle a large population without false matches occurring. Because of this, the threshold can be shifted to the right, $\epsilon \leq 0.20$. By increasing the quality of the enrollment and query iris data provided for the recognition system through modern imaging acquisition technologies. In conclusion, the application of the Hamming, Elias-Bassalygo, and Plotkin upper bounds, along with the Gilbert-Varshamov lower bound, provides researchers a confidence interval of maximum populations in which their iris recognition system can support given the use of Daugman's IrisCode and also a measure of the quality present in the iris images used themselves.

Chapter 3

Measuring Iris Uniqueness Based on Autoregressive Model

1.0 Introduction

As a motivator from Chapter 2, this chapter presents a more generalized approach to measuring iris uniqueness through the use of an iris database's raw data. Similar to Chapter 2 we assume that a one-to-one mapping of each iris class is available, except now we leverage Gaussian codewords verses binary. To start each iris class's power spectral densities are estimated through the use of an Auto-regressive model. Once found, they are implemented in two distance metrics, an asymptotic log-likelihood test and relative entropy. From these distance metric values, we proceed to find the 'best-of-fit' chi-square distributions of their relative frequencies to obtain the degrees of freedom and variance. We base the length of each Gaussian codeword from the fitted degrees of freedom for each metric and then develop a Gaussian Sphere packing bound. We can also leverage these found parameters to develop a similar Daugman-like bound based on a fixed error of enrollment. Through the use of these two developed bounds,

we find the limits on maximum population of two databases: Chinese Academy of Sciences' Institute of Automation (CASIA) CASIA-IrisV3 Interval and University of BATH (BATH) Iris Image Database.

The remainder of this chapter is organized as follows. Section 2.0 presents assumptions and developments of the Auto-regressive model, derivation of the Log-Likelihood and relative entropy metrics, and formulation of the Gaussian Sphere-Packing and Daugman-like Bounds. Section 3.0 provides the implementation of the theory on the two databases. Finally, Section 4.0 gives final conclusions on both bounds presented in this chapter.

2.0 Theory, Model, and Analysis

In this section, we will lay the foundation and assumptions to our methodology for measuring iris uniqueness.

2.1 AR model for vectorized iris images

The autoregressive (AR) model is an example of a stationary random process used to 'forecast' values in time-series data, widely used in weather forecasting. The basic principles of estimation for this model use a linear combination of past values and a stochastic term to introduce variability. We turn to a simple autoregressive model to describe each iris class due to two outstanding properties: it is driven by white Gaussian noise passed into a linear shift-invariant filter, and the model captures dependencies among each iris image per class. Let us begin by making the following assumption. Let there be M enrolled iris classes present in the system, and each class contains N vectorized iris images. Let $X_1^n(m), \dots, X_N^n(m)$ be N vectorized iris images of iris class m , $m = 1, \dots, M$, with superscript n indicating the length of each vector.

Note that in our analysis we treat all vectors as column vectors. Utilizing the theory presented in [31], each entry in an iris class, $X_i^n(m)$, is related through the following AR equation

$$X_t = \sum_{i=1}^p \alpha_i X_{t-i} + W_t, \quad (3.1)$$

where t is a single value in the vectorized iris image, α_i is the estimated coefficient of the model, W_t is a sample of white Gaussian noise process with mean zero and variance σ_W^2 , and p is the parameter that determines the order of the model.

Since we would like to later make use of the frequency domain, using the z-transform, we can easily derive the spectral equations of the linear difference equation as follows

$$X(z) \left(1 + \sum_{i=1}^p \alpha_i z^{-i} \right) = W(z) \quad (3.2)$$

Rewriting 3.2 for $X(z)$, we obtain

$$X(z) = \frac{W(z)}{1 + \sum_{i=1}^p \alpha_i z^{-i}} \quad (3.3)$$

and substituting $z = \exp(j2\pi f_i)$, where we use f to denote frequency, the transfer function can be written as follows

$$H(f) = \frac{1}{1 + \sum_{i=1}^p \alpha_i \exp(-j2\pi f_i)}. \quad (3.4)$$

By knowing the transfer function of the model and the power spectrum of the driving process (which is in our case a white Gaussian noise process with zero mean and variance σ_W^2), we can write an equation of the power spectral density (PSD) of

the data X_t as

$$S_X(f) = \sigma_W^2 |H(f)|^2, \quad (3.5)$$

where $S_X(f)$ is the notation for the PSD on the output of the linear filter.

To estimate our PSDs, we turn to using Burg's Maximum Entropy Method for estimation given in [9] and the following is a brief discussion of the implementation, without mathematical derivations. Here Burg minimizes the sum of forward, f_t^l , and backward, b_t^l , prediction errors, through the use of a recursive algorithm, to obtain reflection coefficients

$$k_l = \frac{-2 \sum_{t=l}^{T-1} f_t^{l-1} b_t^{l-1}}{\sum_{t=l}^{T-1} (f_t^{l-1})^2 + (b_t^{l-1})^2}. \quad (3.6)$$

The Levinson-Durbin algorithm is then implemented using the found reflection coefficients, k_l , to estimate the coefficients given below,

$$\begin{aligned} \alpha_k^l &= \alpha_k^{l-1} + k_l \alpha^{l-1} \quad k = 1, 2, \dots, l-1 \\ \alpha_l^l &= k_l, \end{aligned} \quad (3.7)$$

where $\alpha_0^0 = 1$, $l = 1, 2, \dots, p$, and α_k^p gives the estimated AR coefficients α_k . These AR coefficients are substituted in the transfer function, equation 3.4, to find the PSD estimates for each iris class in equation 3.5. For derivations and a more comprehensive explanation, please refer to [9].

We also turn to the use of Akaike Information Criterion (AIC) to find the optimal order, p , in our AR model. Akaike Information Criterion, is a popular stochastic method for evaluating how well the model's estimated output fits the original data [32]. It measures the trade-off between 'goodness-of-fit' of the model and the model complexity, where too low of a model order causes poor fit into the data, but small complexity, while the choice of a high model order results in a good fit into the data,

but also has high complexity. Akaike derives AIC in [3] as follows,

$$AIC = 2p - 2\log(\hat{L}), \quad (3.8)$$

where p is the model order and \hat{L} is the maximum likelihood over estimated parameter space.

Finally since the AR model is driven by a Gaussian process and is linear, we can make the following realization that each iris vector, $X_i^n(m)$, is also Gaussian:

$$X_i^n(m) \sim \mathcal{N}(\boldsymbol{\mu}(m), \mathbf{K}(m)), \quad (3.9)$$

where $\boldsymbol{\mu}(m)$ is the mean (in our analysis we adjust it to be $\mathbf{0}$) and $\mathbf{K}(m)$ is the covariance matrix of the entries of the i -th vectorized iris image of the m -th class. Thus, each iris class is fitted with a unique AR model.

2.2 Classical Approach to the Estimation of maximum Population

Given probability models for the data of each individual class and for the class dependencies, an optimal approach to the analysis of iris uniqueness is to state the problem of matching a query iris image Y^n to one of M iris classes as an M -ary detection problem [35]. A direct performance analysis for this problem requires forming a $(M - 1)$ dimensional vector of likelihood ratios and evaluating their joint probability density under the assumption that the query data belong to one of M distinct iris classes. Mathematically, performance analysis for this problem becomes quickly intractable, since the expression for the joint probability density function of the vector of likelihood ratios is not straightforward to develop. Furthermore, it is hard to im-

plement in practice. Seeking for an alternative solution, one may turn to an analysis of $M(M-1)/2$ binary detection problems, an approach that is often used in practice. By applying the Union bound [7], the probability of error in an M -ary problem can be upper bounded by a sum of binary error probabilities.

Denote by $P(error)$ the average probability of error in an M -ary detection problem and by $P(error|Class\ m)$ the conditional probability of error, given that data are generated by Class m , $m = 1, \dots, M$. Assuming equal prior probability for each class m , the average probability of error is given as

$$P(error) = \frac{1}{M} \sum_{m=1}^M P(error|H_m). \quad (3.10)$$

After expanding $P(error|H_m)$ as $P(\bigcup_{k=1, k \neq m}^M H_k|H_m)$ and applying the Union bound, the equation above yields

$$P(error) \leq \frac{1}{M} \sum_{m=1}^M \sum_{k=1, k \neq m}^M P(H_k|H_m), \quad (3.11)$$

where $P(H_k|H_m)$ is the error in a binary detection problem for the pair of classes k and m .

The bound (3.11) establishes a link between the total probability of recognition error and the number of iris classes M and thus presents a basis for the analysis of the maximum population of iris biometrics. In spite of being much simplified compared to the original M -ary detection problem, the bound does not yield a general explicit relationship between $P(error)$ and M and becomes hard to evaluate in practice due to a complex nature of practical data.

To take our analysis of the maximum iris population further, in the following subsections, we will first develop an expression for the log-likelihood ratio statistic

and analyze its probability distribution. Then we will return to the bound on $P(\text{error})$ and suggest two alternative approaches that yield an explicit relationship not only between $P(\text{error})$ and M , but also involves the quality of iris data (see [22] for the definitions and standards on iris quality for iris biometrics).

2.3 Log-likelihood Ratio

Given an iris dataset composed of M iris classes, with data of each class being vectorized and then fitted with an AR description, as outlined in Sec. 2.1, the origin of a query vector Y^n can be tested using classical detection theory approaches. Since we have a probability model for data of each class, however parameters of the models are estimated from data, we appeal to Generalized Likelihood Ratio Test (GLRT) [35] to find which of M classes is the origin of vector Y^n . While our peers may find this approach outdated (too classical compared to modern deep learning based approaches), unlike deep learning approaches, this model guarantees an insightful performance analysis, which is a powerful justification within the scope of this work.

Given $M(M - 1)/2$ pairwise binary detection problems to solve, we form a log-likelihood statistic for every pair. For testing the hypothesis “class m is the true class” versus “class k is the true class,” it is given as

$$\Lambda(m, k) = \sum_{j=1}^N \ln \frac{f(Y_j^n | H_m)}{f(Y_j^n | H_k)}, \quad (3.12)$$

where $f(Y_i^n | H_m)$ is the conditional probability density function of the j -th copy of vectorized iris data Y^n , conditioned on class m . After involving the model in (3.9),

the log-likelihood statistic becomes

$$\Lambda(m, k) = -\frac{1}{2} \sum_{j=1}^N Y_j^{nT} (\mathbf{K}^{-1}(m) - \mathbf{K}^{-1}(k)) Y_j^n - \frac{N}{2} \ln \det (\mathbf{K}(m) \mathbf{K}^{-1}(k)). \quad (3.13)$$

The test statistic $\Lambda(m, k)$ is then compared to a threshold to conclude on which class “generated” the vector Y^n . We tentatively set the value of the threshold to zero, since no prior information about the frequency of use of any two classes is available to us, and thus the binary test to perform is given as

$$\Lambda(m, k) \underset{H_m}{\overset{H_k}{\leq}} 0. \quad (3.14)$$

Alternatively, we can vary the value of the threshold in the right hand side of the inequality and analyze $P(H_k|H_m)$ as a function of the threshold.

2.4 Asymptotic Case of Log-likelihood Ratio

When the number of entries in a vectorized iris image is large, that is n is large, (3.13) can be replaced by an asymptotic expression involving the power spectral density of the AR model. It can be easily demonstrated that $\Lambda(m, k)$ in the asymptotic case can be written as

$$\Lambda(m, k) = -\sum_{i=0}^{n-1} \left\{ \left(\frac{1}{S_m(f_i)} - \frac{1}{S_k(f_i)} \right) \sum_{j=1}^N |y_j(f_i)|^2 + N \ln \left(\frac{S_m(f_i)}{S_k(f_i)} \right) \right\} = -\sum_{i=0}^{n-1} \lambda(f_i), \quad (3.15)$$

where y^n is the Fourier transform of Y^n , $S_m(f_i)$ is the i -th sample of the power spectral density of the m -th class (for an insightful explanation of the result see p. 36 of Kay [23]), and $\lambda(f_i)$ is the i -th component of the log-likelihood ratio statistic.

2.5 Analysis of Error Probability, continued

Given a binary detection problem involving two classes, *Class m* and *Class k*, an error will occur in two cases: Case 1: Y^n originated from *Class m*, but $\Lambda(m, k) < 0$; and Case 2: Y^n originated from *Class k*, but $\Lambda(m, k) > 0$. The first case describes $P(H_k|H_m)$, while the second case describes $P(H_m|H_k)$. Both conditional probabilities of error can be expressed in terms of the conditional probability density function of $\Lambda(m, k)$, assuming one or the other class is the true class.

Consider $P(H_k|H_m) = P(\Lambda(m, k) < 0 | \text{Class } m)$. In (3.15), random vector y^n is complex Gaussian under either hypothesis, since y^n is a linear transformation of a Gaussian vector. To find the conditional probability of error $P(H_k|H_m)$, we need a closed form expression for the conditional probability density function (p.d.f.) of $\Lambda(m, k)$ under H_m .

Assuming that y^n is from Class m implies that $y(f_i) \sim \mathcal{CN}(0, S_m(f_i))$, where \mathcal{CN} denotes “complex normal,”

$$y(f_i) \left(\frac{1}{S_m(f_i)} - \frac{1}{S_k(f_i)} \right)^{1/2} \sim \mathcal{CN} \left(0, S_m(f_i) \left(\frac{1}{S_m(f_i)} - \frac{1}{S_k(f_i)} \right) \right)$$

and

$$\lambda(f_i) = \left(\frac{1}{S_m(f_i)} - \frac{1}{S_k(f_i)} \right) \sum_{j=1}^N |y_j(f_i)|^2 + N \ln \left(\frac{S_m(f_i)}{S_k(f_i)} \right)$$

is a N -Erlang random variable with the p.d.f.

$$f_{\lambda(f_i)}(x) = \frac{1}{(\sigma_i^2)^N} \frac{(x - a_i)^{N-1}}{(N-1)!} \exp \left\{ -\frac{(x - a_i)}{\sigma_i^2} \right\}, \quad x > a_i \quad (3.16)$$

where $a_i = N \ln(S_m(f_i)/S_k(f_i))$ and $\sigma_i^2 = 1 - S_m(f_i)/S_k(f_i)$.

The entries $\lambda(f_i)$ in the test statistic $\Lambda(m, k)$ are independent, but not identically

distributed. Therefore, a closed form expression for the conditional pdf of $\Lambda(m, k)$, assuming that the data are generated by *Class* m , is not straightforward to find. At this point, we can take our analysis further by involving the Chernoff bound [35] on $P(H_k|H_m)$. Instead, equipped with the form of the p.d.f. for $\lambda(f_i)$, the well developed theory of error correction codes [11, 24], and a deep insight into Daugman's analysis of IrisCode [15, 13], we reverse the direction of our analysis. In the following two subsections, we analyze the uniqueness of iris biometrics from a perspective of the sphere packing argument [11] and by developing a Daugman like bound [15]. Both provide an explicit relationship of $P(error)$ on the number of classes M and an average quality of iris data in a considered iris dataset.

2.6 Analysis of iris uniqueness using sphere packing argument

As justified in Sec. 2.5, the log-likelihood ratio test statistic is a sum of weighted exponential random variables. While no method for direct evaluation of its p.d.f. is known, a plot of the relative frequency of the log-likelihood statistic can be approximated by a chi-square p.d.f. formed by adding K iid squared complex Gaussian random variables each with zero mean and variance P . The parameter K is the number of degrees of freedom of the fitted chi-square p.d.f. Since K and P are unknown, they must be estimated from empirical data.

The fitted chi-square p.d.f. allows us to interpret the problem of finding the maximum iris population as a Gaussian sphere packing result. Suppose an encoding strategy is available to map ideal iris images (iris images with no noise or distortions) of M distinct iris classes into unique Gaussian codewords, each of length K . Each codeword is drawn i.i.d. from a Gaussian distribution with zero mean and variance

P . Suppose further that an iris image of one of M classes (for example, of Class m) submitted for authentication or recognition is modeled as a noisy version of the ideal codeword of Class m . The noise is zero mean Gaussian with variance N in each of K dimensions. Thus, for a given Class m the iris image submitted for authentication is mapped into a point within a K -dimensional sphere with radius \sqrt{KN} around the codeword of Class m . Since the Gaussian sphere containing codewords of M classes has radius $\sqrt{K(P+N)}$, the maximum number of classes, assuming that the distortion of iris images submitted for authentication is bounded, can be obtained by dividing the volume of a K dimensional sphere containing all codewords by the volume of the small sphere representing noise in the data of particular iris class. Thus,

$$M \leq \left(1 + \frac{P}{N}\right)^{K/2}. \quad (3.17)$$

See [11] for a more insightful description.

2.7 A Daugman-like approach to the analysis of iris uniqueness

Similar to the sphere packing argument presented in the previous section, Daugman-like analysis of iris uniqueness is based on the assumption that data of iris classes are mapped into a space in which each iris class is presented by an independent Gaussian codeword of length K with zero mean and variance P , where K and P are defined above. This mapping ensures that the asymptotic pairwise log-likelihood ratios (here interpreted as a distance between two codewords) are independent chi-square distributed random variables with K degrees of freedom. The asymptotic log-likelihood ratio can be also replaced with an estimate of the relative entropy between the p.d.f.s

of two iris classes. This leads to a new interpretation of the distance measure as a means to also measure the quality of iris data. Its introduction allows a rate-distortion interpretation of the problem of finding the maximum iris population that an iris recognition system can sustain, similar to how error-correction bounds in coding theory relate the maximum population of binary code to the minimum Hamming distance between codewords [24]. To be specific, the introduction of such metric will lead to a new performance bound that relates the size of iris population covered by the recognition algorithm and the quality of iris biometric data, while ensuring a small probability of recognition error.

At this point of our analysis, in addition to the asymptotic log-likelihood ratio statistic we introduce the relative entropy between the probability density functions of two classes m and k . The relative entropy is defined as the expected value of the log-likelihood ratio in (3.15)

$$d(m, k) = \mathbb{E} [\Lambda(m, k)] = \sum_{i=0}^{n-1} \left\{ \frac{S_m(f_i)}{S_k(f_i)} - \ln \frac{S_m(f_i)}{S_k(f_i)} - 1 \right\}, \quad (3.18)$$

where \mathbb{E} is the notation for the expected value operator. Since the power spectral densities of different iris classes are not known to us, they are first estimated from available class data and then plugged in the expression for the relative entropy in place of the true unknown power spectral densities.

With estimated relative entropy as a distance metric, the bound on the maximum population of enrolled iris population is straightforward to develop. We follow an argument similar to Daugman's that the imposter distance between a pair of distinct iris classes can be fitted with a chi-square pdf with K degrees of freedom. Then the

error to enroll can be mathematically described as

$$P(\text{error to enroll}) = 1 - P\left(\bigcap_{m=1}^M d(m, M+1) > T\right), \quad (3.19)$$

where $d(m, M+1)$ is the distance between a previously successfully enrolled class m and a new (not yet enrolled) class $M+1$. Since pairwise distances between iris classes are independent identically distributed chi-square random variables, (3.19) can be rewritten as

$$P(\text{error to enroll}) = 1 - \{1 - P(d(m, M+1) \leq T)\}^M \leq \delta, \quad (3.20)$$

Inverting the inequality for M results in

$$M \leq \frac{\log(1 - \delta)}{\log\{1 - FMR(T)\}}, \quad (3.21)$$

where $P(d(m, M+1) \leq T)$ is replaced with $FMR(T)$, abbreviation for False Match Rate as a function of the distance between two codewords T .

3.0 Illustration

The following section describes our application of the theory presented above to find the maximum population of two datasets. The flow of our methodology is shown in figure 3.1.

3.1 Data

Chinese Academy of Sciences' Institute of Automation (CASIA) CASIA-IrisV3 Interval [10] and University of Bath (BATH) Iris Image Database [26] are used to

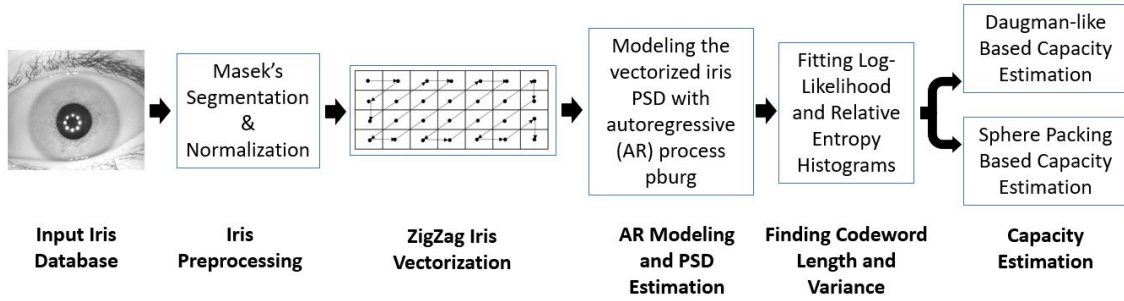
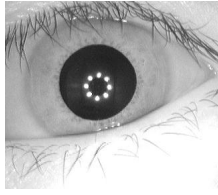


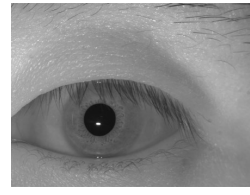
Figure 3.1: A block diagram of the proposed methodology.

demonstrate our proposed methodology. Although any database may be used to demonstrate our methodology, we choose these databases due to their high-quality of iris images available and the differences in iris texture; where the BATH database is composed of European irises with high texture located throughout the iris, and CASIA-IrisV3 Interval is composed of Asian irises with very fine texture located closely towards the pupil. The CASIA-IrisV3 Interval contains 2,639 near infrared (NIR) illuminated images, each having a resolution of 320x280 pixels, and a total of 249 subjects (498 classes with each subject's left and right eye being independent classes). The BATH database contains 32,000 NIR iris images with 800 subjects, however a smaller portion of this dataset is used as the larger dataset is no longer publicly available. Therefore, the smaller 'sample' BATH dataset contains 1,000 images, each with resolution 960x1280 pixels, and 25 subjects or 50 independent classes (with each subject having 20 images for both the left and right eye).

Through using high-quality data, we hope to obtain the best measure of iris uniqueness possible. Because the collection of iris images is not perfect, the iris classes with large errors (such as occlusions, illumination errors, blur, motion, etc.) present throughout the class are discarded for both datasets to ensure that we are



(a) Example excluded image from CASIA dataset.



(b) Example excluded image from BATH dataset.

Figure 3.2: Example iris images from CASIA (3.2a) and BATH (3.2b). 3.2a shows both upper occlusion, from eyelashes, and lower occlusion, from eyelid. 3.2b shows dominate eyelash occlusion.

measuring uniqueness based off of iris texture alone. For the first step of data reduction, each class is manually inspected for errors that consume over half of the iris texture, mainly looking at occlusions such as eyelashes and eyelids. Figure 3.2 shows an example iris class from each database that had major occlusions present throughout its images collected.

After excluding these classes, further data reduction is performed on each dataset to ensure that there are an equal number of images per iris class to reduce bias. For the BATH database, this is not a concern as 20 images were collected for each iris class, however for CASIA-IrisV3 Interval, the number of images per class varied, from as low as 4 to as high as 20. To ensure that we had enough images and classes for analysis, we eliminated classes that had less than 10 images and for the classes that had greater than 10, we only extracted 10 images randomly from that class. Through this simple reduction procedure, we are left with 21 classes in the CASIA-IrisV3 Interval database, with each class containing 10 images, and 40 classes for the BATH database, with 20 images per class. Tables 3.1 and 3.2 summarize the reduction of data for each database. This smaller set of data for each database is used to demonstrate our methodology.

Table 3.1: Data reduction performed on CASIA-IrisV3 Interval Database.

	Original	Reduced
Independent Classes	498	21
NIR Images per Class	4-20	10
Resolution (pixels)	320x240	320x240

Table 3.2: Data reduction performed on smaller BATH Database.

	Original	Reduced
Independent Classes	50	40
NIR Images per Class	20	20
Resolution (pixels)	960x1280	960x1280

3.2 Libor Masek Segmentation and Preprocessing Steps

To obtain the correct format of our data to implement in the AR model, we turn to Libor Masek’s open-source iris recognition algorithm [25]. Although this algorithm is simplistic, it is a widely accepted program that is easy to understand and produces robust results. While Masek proposes an end-to-end iris recognition system, we only want to utilize his developed tools of segmentation, normalization, and his method of Log-Gabor filtering. To begin, Masek’s segmentation code is tuned to each database, changing the iris and pupil search radius and sensitivity parameters, and each iris image contained in both subset databases are segmented. From here, we use Masek’s normalization method to unwrap the segmented irises from polar coordinates, ‘doughnut’ shape, to a fixed dimension, in our case 20x240 pixels. For a more detailed description of Masek’s implementation please see [25].

Once each iris image is correctly segmented and normalized, we crop each normalized image by 50% and retain the texture that is closest to the pupil. This further data reduction is preformed as another check to be certain that we are measuring the

irises' uniqueness through texture and discards any additionally missed occlusions from masking during segmentation. After cropping, the resulting normalized image size for each iris is 10x240 pixels. The next step of preprocessing the data is filtering each now cropped normalized image with a 1-D Log-Gabor filter. The same filter implementation is used from Masek's codes, and in Section 3.3.1 the affects of the filter's center frequency and bandwidth on the cropped normalized iris images are analyzed. Figure 3.3 shows the processing steps of a single iris image.

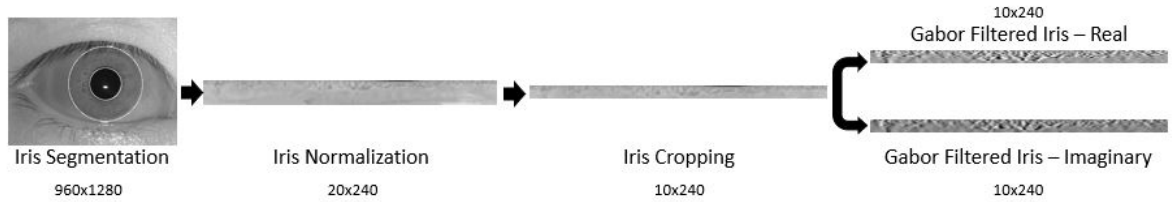


Figure 3.3: Example segmentation and pre-processing steps of a single BATH iris image before ZigZag vectorization is preformed.

Once the Log-Gabor filtered iris image is obtained, the complex-valued image is unwrapped using what we call ZigZag vectorization. This method first unwraps the real-valued filtered image into a one dimensional vector by applying a diagonal scan from the top left corner of the image to its bottom right corner, as seen in Figure 3.4. The same unwrapping is applied to the imaginary-valued filtered image. Once both the real-valued and imaginary-valued filtered images are vectorized from a 2D matrix to a 1D vector, the imaginary-valued 1D image is concatenated onto the end of the real-valued 1D image (for our data the total vector length is 4,800 pixels). This ZigZag vectorization method was adapted to preserve the spatial correlation of the iris patterns while transitioning the 2D image to a 1D representation. ZigZag was introduced in [20] and previously effectively used in combination with Discrete Cosine Transform to accomplish lossy compression. It was also adopted in application

3.3 Estimation of Power Spectra

As stated in Sec. 2.1, to ensure a workable model that can be used to analyze performance of iris biometrics, we turn to an Auto Regressive (AR) model for the vectorized iris data. The analysis of maximal population is based on a successful implementation of (3.15) and (3.18) which in turn rely upon estimates of the power spectral densities obtained from data of iris classes. These estimates are found through 1.) finding the optimal order for the AR model given our iris data, 3.3.1 and 2.) using Burg's Maximum Entropy Method to find high quality spectral estimates for each iris class, 3.3.2. Sections 3.3.3 and 3.3.4 show the justifications for choosing our method of vectorization and the use of the AR model to obtain estimates for each iris class.

3.3.1 Finding Optimal Model Order

Estimating the appropriate model order is essential in the performance of the AR model. Having a large order ensures a better fit into data, however it also increases complexity of the implementation and can lead to overfitting of noise. To achieve a balance between approximation and estimation error we involve Akaike Information Criterion (AIC) in conjunction with the AR method in MATLAB to find the optimal model order of estimated power spectra.







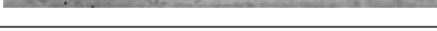
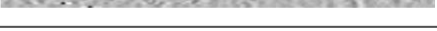


SUBJECT	NORMALIZED	GABOR FILTERED
199R		
81R		
19L		
53R		
104L		

Figure 3.5: Subset of CASIA-IrisV3 Interval dataset that is used to see if texture had an affect on optimal AR model order. Subjects are chosen by varying texture, with Subject 199R having very fine texture to Subject 104L having very rough texture. Only the Real-Valued Gabor Filtered Irises are shown here, due to the high similarities between the real-value and imaginary-value portions of the complex image.

To begin, a subset of iris classes were extracted from each dataset based on varying texture levels, from very fine to rough texture, to see if the structure of the iris affects model order. Figures 3.5 and 3.6 show the hand selected iris classes from both the CAISA-IrisV3 Interval and BATH datasets. Upon initial run of finding the optimal order for each dataset, the Average AIC plots for each dataset showed a stair-steppingg' behavior, shown in Figure 3.7. These plots were not useful in determining the correct order to fit our iris data due to their varying nature. Because of this, we explore Masek's 1-D Log-Gabor filter parameters of center frequency, f_0 , and bandwidth, σ , and their affect on the performance of AIC for each set.











SUBJECT	NORMALIZED	GABOR FILTERED
13L		
19R		
7R		
2R		
17R		

Figure 3.6: Subset of BATH dataset that is used to see if texture had an affect on optimal AR model order. Subjects are chosen by varying texture, with Subject 13L having very fine texture to Subject 17R having very rough texture. Only the Real-Valued Gabor Filtered Irises are shown here, due to the high similarities between the real-value and imaginary-value portions of the complex image.

In Masek’s open-sourced iris recognition algorithm, [25], he implements a simple Log-Gabor Filter for the use of edge detection/enhancement in the normalized iris image. While he uses multiple resolutions of Log-Gabor Filters, due to his encoding method similar to Daugman’s [17], we are only interested in one resolution. Because of this, we simply implement the following Log-Gabor transfer function on each raw normalized iris,

$$G(f) = \exp \left\{ -\frac{1}{2} \left(\frac{\log(f/f_0)}{\log(\sigma/f_0)} \right)^2 \right\}, \quad (3.22)$$

where f_0 is the center frequency and σ is the bandwidth of the filter. Each normalized image is filtered using the same f_0 and σ throughout the entire dataset for consistency, and then the filtered images power spectral densities are estimated using Burg’s AR method to find the ‘best of fit’ model order.

To begin to understand the affects of the Log-Gabor parameters on the AIC for each iris class, extensive search simulations are designed to look at the impact of the center frequency and bandwidth on the quality of the images themselves. Since the

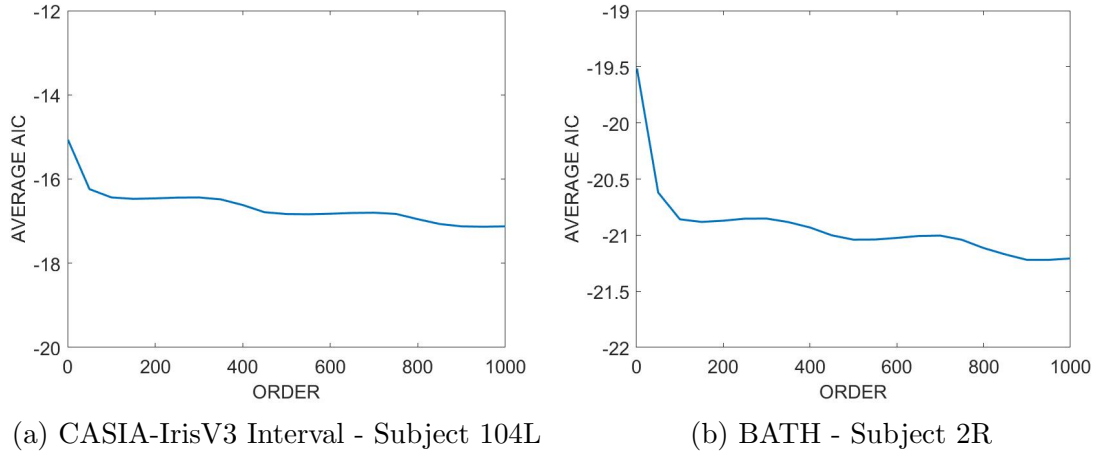


Figure 3.7: Plots of initial average AIC values for a single class for both datasets using original Masek Log-Gabor Filter parameters of $f_0 = 1/18$ and $\sigma = 0.5$. Both plots show the unwanted stair-stepping behavior occurring across all classes average AIC plots.







Figure 3.8: Reference normalized and cropped iris image for analyzing Gabor filter performance.

Log-Gabor Filters behave as edge detectors, starting the simulations we are looking at both the quality of enhancement the filter was performing on the images themselves (enhancing the texture within the iris itself) and the overall impact on the AIC curves to find the optimal order of the AR model. For each dataset, the simulations are performed on the subset of irises already extracted by varying texture, Figures 3.5 and 3.6, however, for simplicity, the following results plotted are of one iris class from each dataset: Subject 104L for CASIA-IrisV3 Interval and Subject 2R for BATH. Figure 3.8 shows the normalized and cropped iris images from Libor Masek's algorithm for each iris class.






Picking a Resolution: Based off of the 'Decidability Studies' conducted by Masek in [25], where the correlation of different center frequency values (resolutions) are

analyzed to find the most independent values for his encoding process, the center frequency values chosen for our study are varied by factors of $1/9$, as these produced the highest decidability scores. Odd values of the bandwidth are chosen, from 0.1 to 0.9, to also analyze the performance on iris quality. Figure 3.9 and 3.10 shows an example of one iris for each dataset and the varying image quality as f_0 and σ change. From the figures, we can see that as the bandwidth of the filter increases, the edges of the iris becomes sharper and sharper to the point in which it becomes unrecognizable as a normalized iris image. We can also observe that as the center frequency increases, the normalized iris image becomes more pixelized and blurry. Due to the texture degregation, the AIC plots analyzed are only the bandwidths of 0.1, 0.3, and 0.5, along with a lower center frequency of $1/9$. These results are shown in Figures 3.11 and 3.12 for both datasets. From both figures, we can see that as the bandwidth increases, the stair-stepping behavior diminishes. Because of this and the visible iris image quality, our initial pick for center frequency and bandwidth is $f_0 = 1/9$ and $\sigma = 0.5$.






Analyzing lower center frequencies: To make sure we have have the best choice for center frequency and bandwidth, we perform another extensive search keeping our bandwidth fixed, $\sigma = 0.5$, and varying our center frequency around $f_0 = 1/9$. For the purpose of illustration, the figures shown only display center frequencies of $f_0 = 1/3$, $f_0 = 1/6$, $f_0 = 1/9$, and $f_0 = 1/12$ to show the impact that center frequency plays in the best fit of our AR model. Figures 3.13 and 3.14 show the new filtered normalized iris images. We can see from both figures that the iris texture goes from extremely sharp to more blurry as the center frequency is increased. Figures 3.15 and 3.16 show the newly plotted average AIC values for each chosen center frequency. These plots confirm that a center frequency of $f_0 = 1/9$ and a bandwidth of $\sigma = 0.5$ produce the richest filtered iris image, along with the most stable average AIC plots.

Bandwidth (σ)	Real-Valued Gabor Filtered Iris Image
0.1	
0.3	
0.5	
0.7	
0.9	






(a) $f_0 = 1/9$

Bandwidth (σ)	Real-Valued Gabor Filtered Iris Image
0.1	
0.3	
0.5	
0.7	
0.9	

(b) $f_0 = 1/18$






Bandwidth (σ)	Real-Valued Gabor Filtered Iris Image
0.1	
0.3	
0.5	
0.7	
0.9	

(c) $f_0 = 1/27$






Bandwidth (σ)	Real-Valued Gabor Filtered Iris Image
0.1	
0.3	
0.5	
0.7	
0.9	

(d) $f_0 = 1/36$






Figure 3.9: Varying center frequencies, f_0 , of CASIA-IrisV3 Interval sample subject 104L. As bandwidth, σ , of Log-Gabor filter is varied, along with center frequency, the normalized iris image's edges become sharper and sharper. Optimal initial center frequency and bandwidth is $f_0 = 1/9$ and $\sigma = 0.5$ by inspection.

Bandwidth (σ)	Real-Valued Gabor Filtered Iris Image
0.1	
0.3	
0.5	
0.7	
0.9	






(a) $f_0 = 1/9$

Bandwidth (σ)	Real-Valued Gabor Filtered Iris Image
0.1	
0.3	
0.5	
0.7	
0.9	

(b) $f_0 = 1/18$

Bandwidth (σ)	Real-Valued Gabor Filtered Iris Image
0.1	
0.3	
0.5	
0.7	
0.9	

(c) $f_0 = 1/27$

Bandwidth (σ)	Real-Valued Gabor Filtered Iris Image
0.1	
0.3	
0.5	
0.7	
0.9	

(d) $f_0 = 1/36$

Figure 3.10: Varying center frequencies, f_0 , of BATH sample subject 2R. As bandwidth, σ , of Log-Gabor filter is varied, along with center frequency, the normalized iris image's edges become sharper and sharper. Optimal initial center frequency and bandwidth is $f_0 = 1/9$ and $\sigma = 0.5$ by inspection.

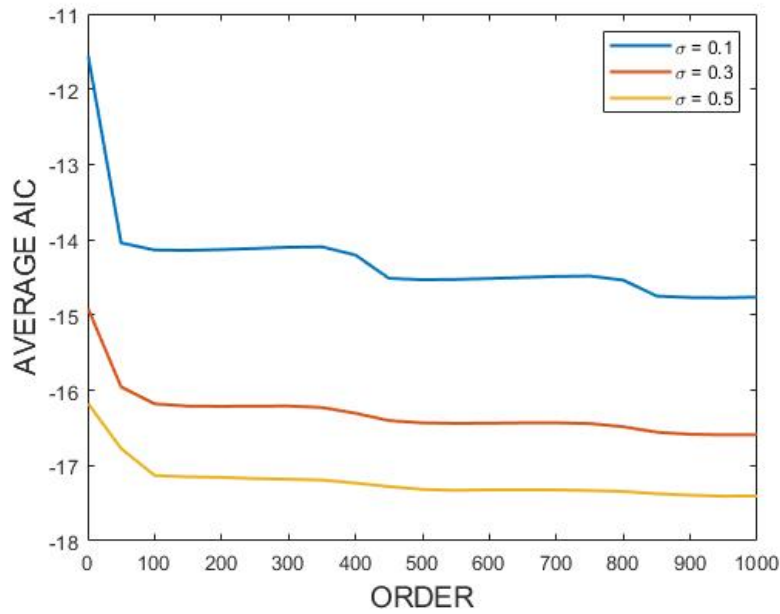


Figure 3.11: Average AIC plots for CASIA-IrisV3 Interval subject 104L given a center frequency of $f_0 = 1/9$ and varying bandwidths of $\sigma = 0.1$, $\sigma = 0.3$, and $\sigma = 0.5$.

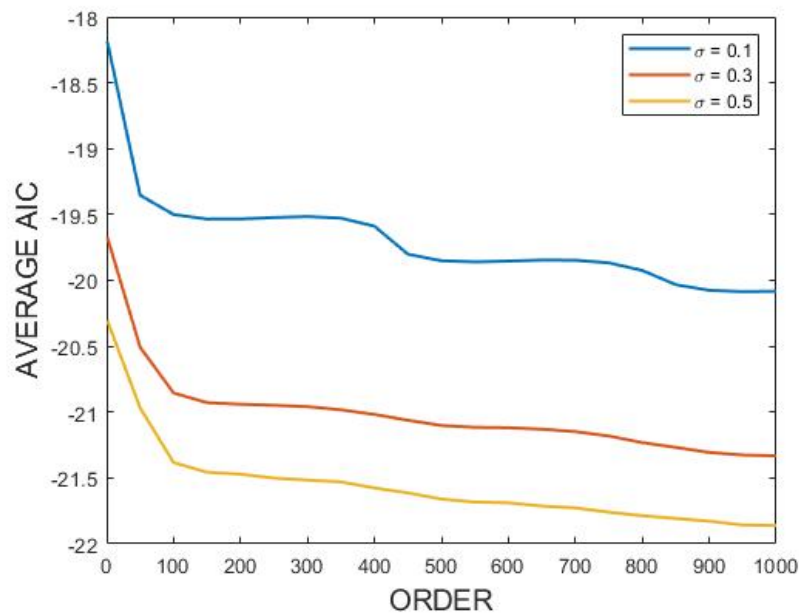


Figure 3.12: Average AIC plots for BATH subject 2R given a center frequency of $f_0 = 1/9$ and varying bandwidths of $\sigma = 0.1$, $\sigma = 0.3$, and $\sigma = 0.5$.





Center Frequency (f_0)	Real-Valued Gabor Filtered Iris Image
1/3	
1/6	
1/9	
1/12	

Figure 3.13: Log-Gabor Filtered iris image for subject 104L from CASIA-IrisV3 Interval with varying center frequencies of $f_0 = 1/3$, $f_0 = 1/6$, $f_0 = 1/9$, and $f_0 = 1/12$ and a fixed bandwidth of $\sigma = 0.5$.





Center Frequency (f_0)	Real-Valued Gabor Filtered Iris Image
1/3	
1/6	
1/9	
1/12	

Figure 3.14: Log-Gabor Filtered iris image for subject 2R from BATH with varying center frequencies of $f_0 = 1/3$, $f_0 = 1/6$, $f_0 = 1/9$, and $f_0 = 1/12$ and a fixed bandwidth of $\sigma = 0.5$.

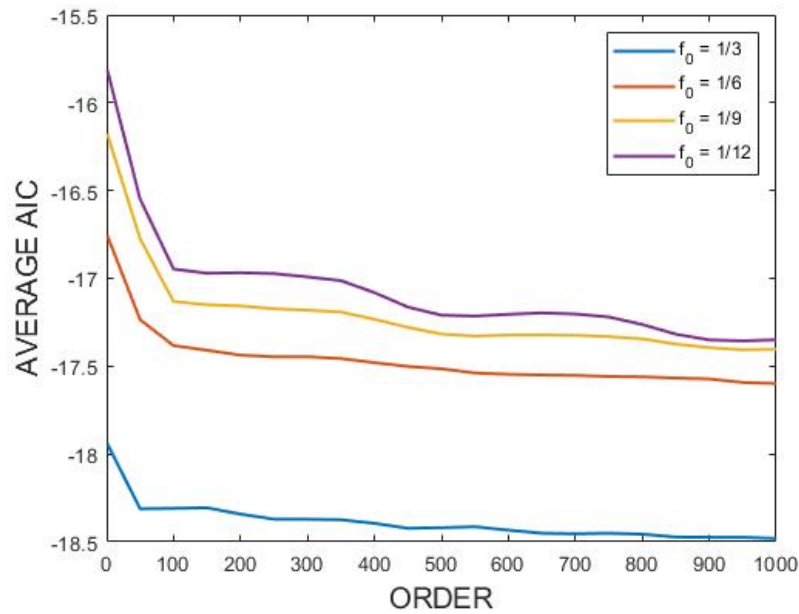


Figure 3.15: Average AIC plots for CASIA-IrisV3 Interval subject 104L given a varying center frequency of $f_0 = 1/3$, $f_0 = 1/6$, $f_0 = 1/9$, and $f_0 = 1/12$, with a fixed bandwidth of $\sigma = 0.5$.

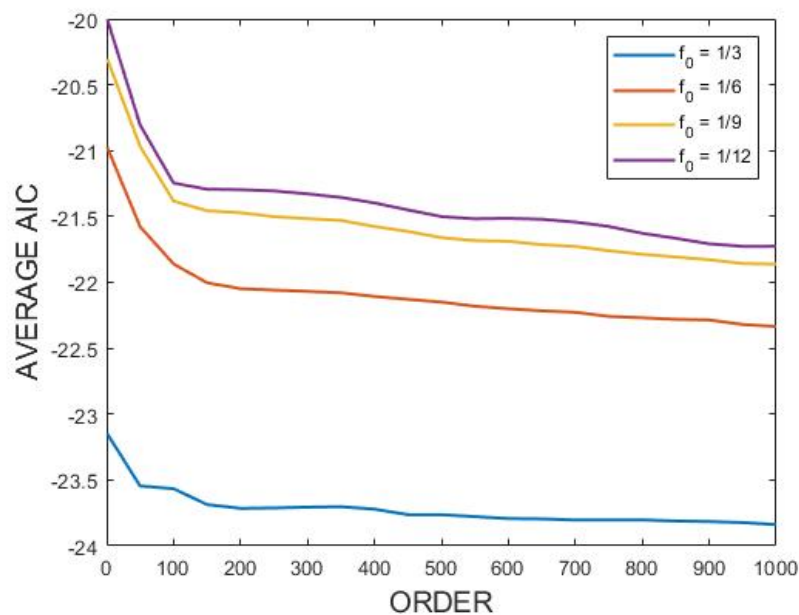


Figure 3.16: Average AIC plots for BATH subject 2R given a varying center frequency of $f_0 = 1/3$, $f_0 = 1/6$, $f_0 = 1/9$, and $f_0 = 1/12$, with a fixed bandwidth of $\sigma = 0.5$.

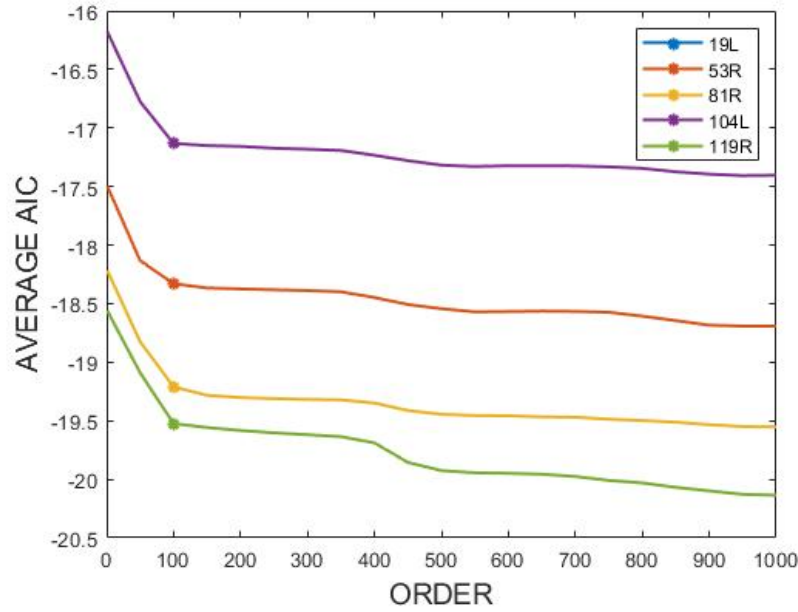


Figure 3.17: Average AIC plots for subset of varying textured irises from CASIA-IrisV3 Interval with fixed Log-Gabor Filter parameters of $f_0 = 1/9$ and $\sigma = 0.5$. Plots demonstrate that varying texture of the iris does not affect the optimal model order of 100. Subject 19L and 53R have the same average AIC plots and overlap (as seen in the figure).

Choosing Optimal Order: After finding the center frequency and bandwidth that minimizes the stair-stepping affect and has the richest filtered iris texture, the optimal order can be approximated from the resulting average AIC plots. Figures 3.17 and 3.18 show the AIC plots for both datasets' subset of different texturized iris images, from Figures 3.5 and 3.6. The resulting plots demonstrate that the optimal order for both datasets is 100, where the average AIC values converge. We can also conclude that each class can be parameterized by the same model order, regardless of iris texture, and that choosing a higher order leads to the same performance as an order of 100. For the remainder of the work, a model order of 100 will be used in finding the estimated power spectral densities for each class.

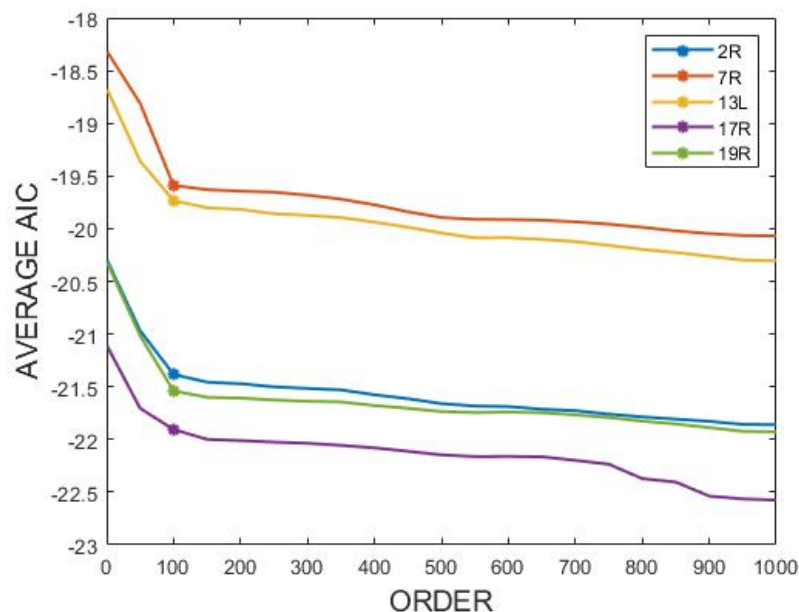


Figure 3.18: Average AIC plots for subset of varying textured irises from BATH with fixed Log-Gabor Filter parameters of $f_0 = 1/9$ and $\sigma = 0.5$. Plots demonstrate that varying texture of the iris does not affect the optimal model order of 100.

3.3.2 AR Implementation

Burg's Maximum Entropy Method [9] is implemented to estimate high-quality spectral densities for each iris subject through the use of MATLAB's Signal Processing Toolbox function *pburg* (with the found optimal order from 3.3.1 as the model order input). An estimated sample from each database is shown in Figure 3.19. After the PSDs are estimated for each image in each class, the data within each class is partitioned into two categories: query and enrollment. To begin, each class's number of PSDs are divided by 50% ($n/2$), half going to enrollment and the other half to query. This leaves 5 images for query and enrollment in the CASIA-IrisV3 Interval dataset per class and 10 images for query and enrollment in the BATH dataset per class. To find the enrollment PSD, all $n/2$ (5 or 10) PSDs are simply averaged. The query PSDs are also an average of the available data by taking the average of each

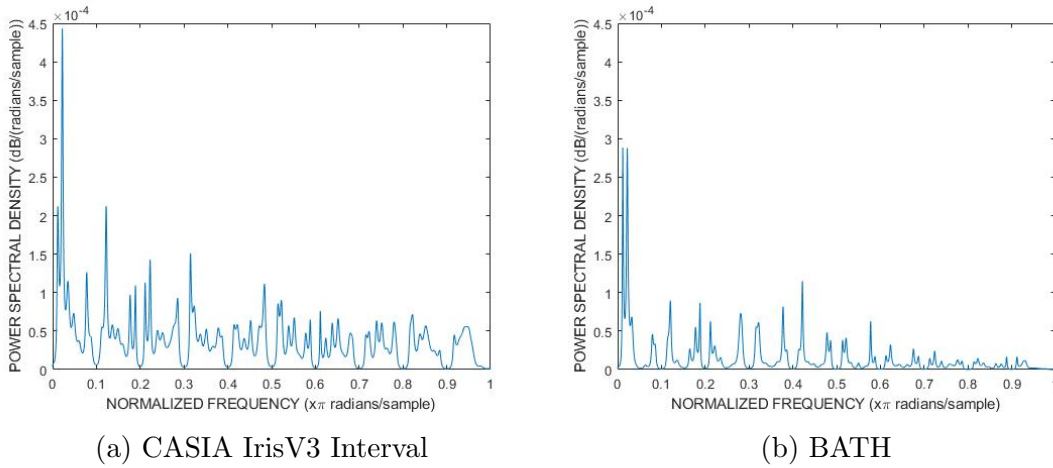


Figure 3.19: Estimated Power Spectral Densities for both datasets through the use of MATLAB’s *pburg* method.

independent combination of PSDs, $n/2 C_{n/2-1}$. These estimates are used in (3.15) and (3.18), where S_m and S_k represent the enrollment PSDs for class m and k and y_j represents the query PSDs, to empirically find the maximum population given the sphere packing bound and Daugman-like bound, shown in 3.5 and 3.6.

3.3.3 Justification of ZigZag Iris Unwrapping Methodology

While other methods look at the normalized iris row by row, and unwrap by using the method shown in Figure 3.20, this loses spatial dependencies between the rows themselves and contributes discontinuities between each row concatenation. Because of this, we choose the zigzag method of unwrapping to keep the spatial correlation between the textures in the iris. Keeping these dependencies also decreases the total probability of error when using our log-likelihood measure. To test this, we unwrap our normalized iris images using both our zigzag vectorization and row-by-row presented in Figure 3.20. Using the complete BATH dataset, we ran two independent experiments, finding the likelihoods using the zigzag vectorization and using the row-by-row vectorization. From here, the total probability of error is analyzed by finding

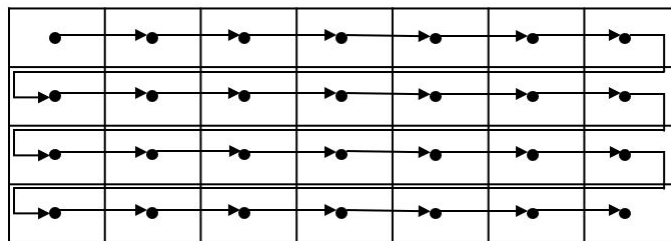


Figure 3.20: Row-by-row vectorization.

all Type I and Type II errors and dividing by the total number of likelihoods found. From these experiments, we find that using the zigzag vectorization the total percent error is 8.4% and by using the row-by-row vectorization, the total percent error is 48.2%.

3.3.4 Proving Shift-Invariance of AR Model on Estimated Power Spectral Densities

An advantage to using the Autoregressive model, to find the power spectral density estimates for each iris image, is that it provides shift-invariance. Shift-invariance is important due to the positioning of the iris in the image itself and can compensate for tilting of the head when the image is taken or when the iris is segmented (as the location of unwrapping the iris image would be different between a tilted head vs. untilted head). Because of this, we want to justify that the model is shift-invariant. To achieve this, we look at the subset of iris images from the BATH dataset that varies by texture. From here, we unwrap the images using the zigzag vectorization and shift the values by 1, 10, and 100 and compare these estimated PSDs against the original estimated PSDs. Figure 3.21 shows the newly estimated PSDs against the original from a single iris image from subject 2R in the BATH dataset. We can see that as the shift is increased, this only has a slight affect on the magnitude of the PSDs while the shape remains the same. The maximum total error between the

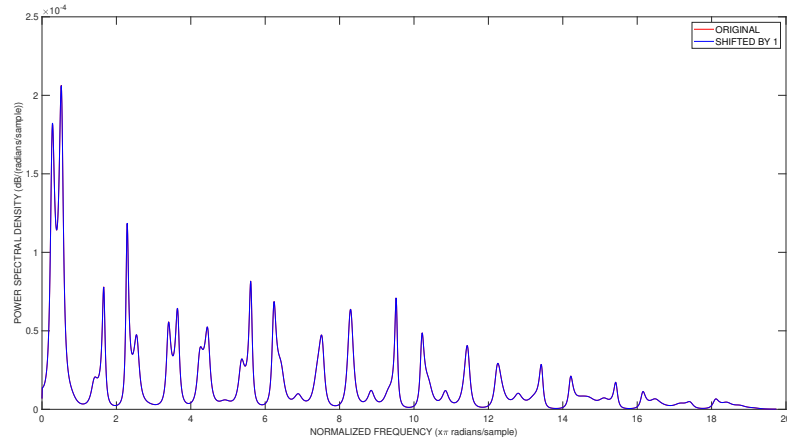
shifted PSD and original PSD is 9.3956×10^{-4} and occurs from the shift of 100. From this small experiment, we can see that the AR model is indeed shift-invariant and makes our methodology more robust to slight variations when the iris is captured.

3.4 Fitting Relative Frequency Distributions

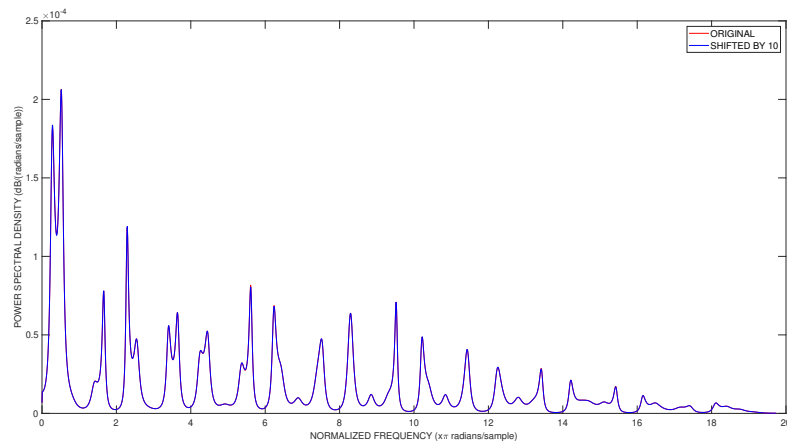
For both bounds presented in this chapter, equations 3.17 and 3.21, the empirical values for K and P must be found for both databases. We achieve this by fitting the imposter relative frequencies, where the estimated PSDs S_m and S_k are from different classes, with the following chi-square probability distribution,

$$f(x; K) = \begin{cases} \frac{x^{(K-2)/2}}{2^{K/2}\Gamma(K/2)} \frac{1}{P^{K/2}} \exp\left(-\frac{x}{2P}\right), & x > 0 \\ 0, & \text{otherwise} \end{cases} \quad (3.23)$$

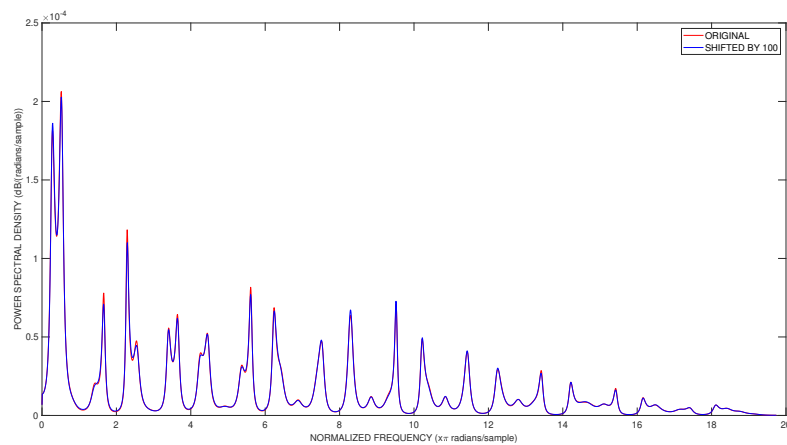
where K is the degrees of freedom, P is the variance of the zero mean Gaussian distributions, and x is our distance metric values, from zero to maximum value for both log-likelihood and relative entropy values. To find the best-of-fit chi-square distribution for our histograms, we perform an extensive search algorithm to find the degrees of freedom and variance that produces the minimum least square error between the fitted distribution and the original histogram. Figure 3.22 shows the best-of-fit chi-square distributions for both the CASIA-IrisV3 Interval and BATH databases using the relative entropy metric from equation 3.18. Here we can see that both databases have an optimal degrees of freedom of $K = 4$ and separate variances of $P_{CASIA} = 252$ and $P_{BATH} = 383$. Figure 3.23 displays the best-of-fit distributions for both databases using the log-likelihood values found from equation 3.15. From these distributions, we can see that CASIA-IrisV3 Interval has an optimal degree of freedom of $K = 4$ and variance $P_{CASIA} = 106$, while the BATH database has a



(a) Shifted by 1



(b) Shifted by 10



(c) Shifted by 100

Figure 3.21: Estimated power spectral densities of on iris image from the BATH shifted by 1, 10, and 100 pixels compared again the original estimate.

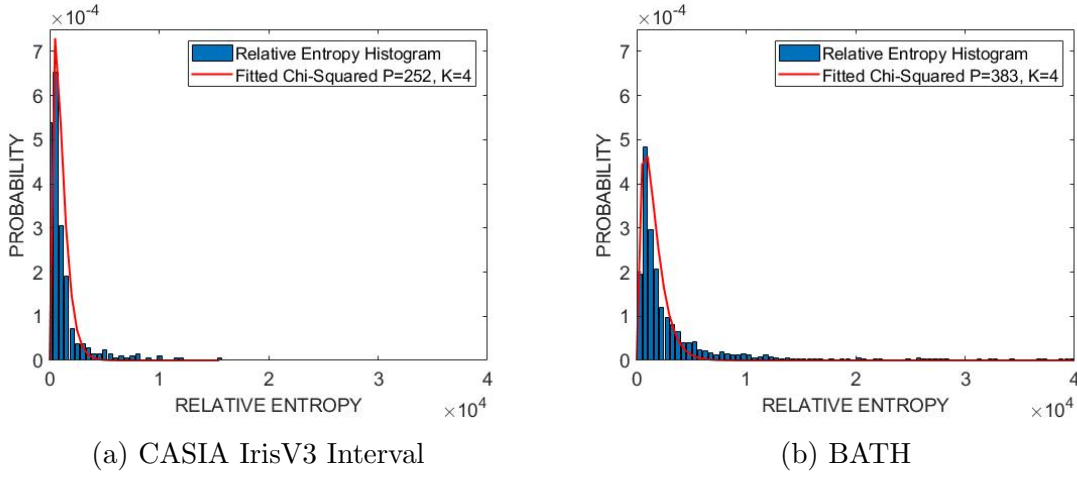


Figure 3.22: Relative Entropy Imposter distributions for both datasets with best-of-fit chi-square distributions. CASIA-IrisV3 Interval having $K = 4$ degrees of freedom and a fitted variance of $P = 252$, shown in (a), and BATH having $K = 4$ degrees of freedom and a fitted variance of $P = 383$, shown in (b).

different degree of freedom of $K = 3$ and a variance of $P_{BATH} = 216$ that produces the best fit. From these found K and P values, we can now find the bounds on maximum population for each dataset using equation 3.17 for the Gaussian Sphere Packing bound, shown in Section 3.5, and equation 3.21 for the Daugman-like bound, shown in Section 3.6.

3.5 Sphere Packing Bound

This section describes the illustration of our developed Sphere-Packing Bound from Section 2.6 to evaluate the maximum population of our two databases, CASIA-IrisV3 Interval and BATH. Here, the maximum population sustainable, M , is dependent on the variance of the gaussian in-which the codewords are drawn, P , the length of the codeword, K , and the noise variance for each class, N . Using our results from the previous section, Section 3.4, we can use our best-of-fit degrees of freedom, K , and variance, P , from both the log-likelihood metric and relative entropy values

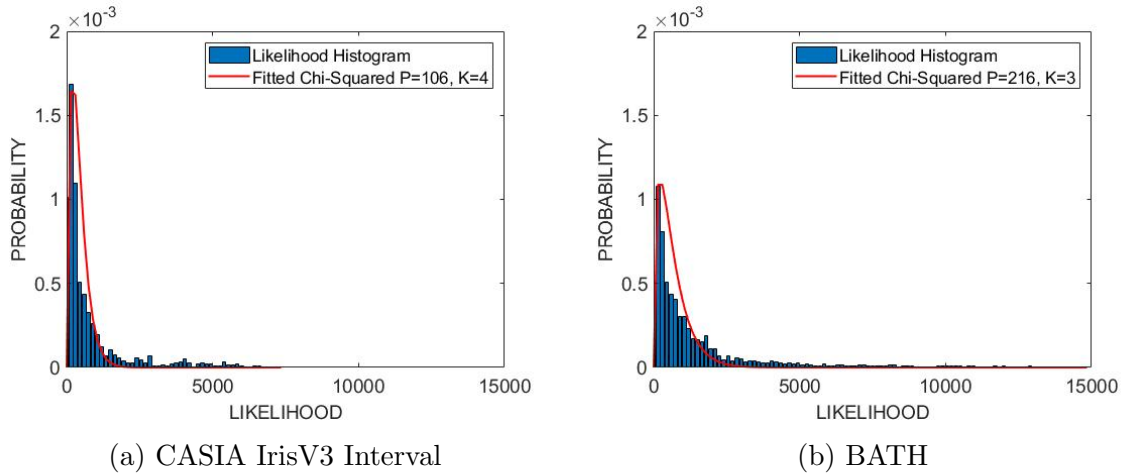


Figure 3.23: Likelihood Imposter distributions for both datasets with best-of-fit chi-square distributions. CASIA-IrisV3 Interval having $K = 4$ degrees of freedom and a fitted variance of $P = 106$, shown in (a), and BATH having $K = 3$ degrees of freedom and a fitted variance of $P = 216$, shown in (b).

obtained between models. As for the noise variance, N , it is varied to reflect possible variance values (from little to extremely noisy images), as there is no simple method in which to find the noise present. Figure 3.24 shows the resulting bound, dependent on increasing noise variance, for CASIA-IrisV3 Interval (a) and BATH (b) databases using the fitted log-likelihood histogram values. Figure 3.25 shows similar plots of the Sphere-Packing Bound, except uses the fitted relative entropy histogram values. Table 3.3 gives a subset of empirical maximum populations dependent on a given noise variance present in an iris class.

Looking at the subset of values presented in Table 3.3, given the absolute lowest value for noise variance, N , the CAISIA-IrisV3 Interval can support a maximum population of $M = 6.40 \times 10^4$ classes for relative entropy and $M = 1.15 \times 10^4$ classes for likelihoods, while the BATH database can sustain $M = 1.48 \times 10^5$ classes for relative entropy and $M = 3.2 \times 10^3$ classes. Intuitively, since the BATH database is of higher quality than the CASIA-IrisV3 Interval database, the maximum population

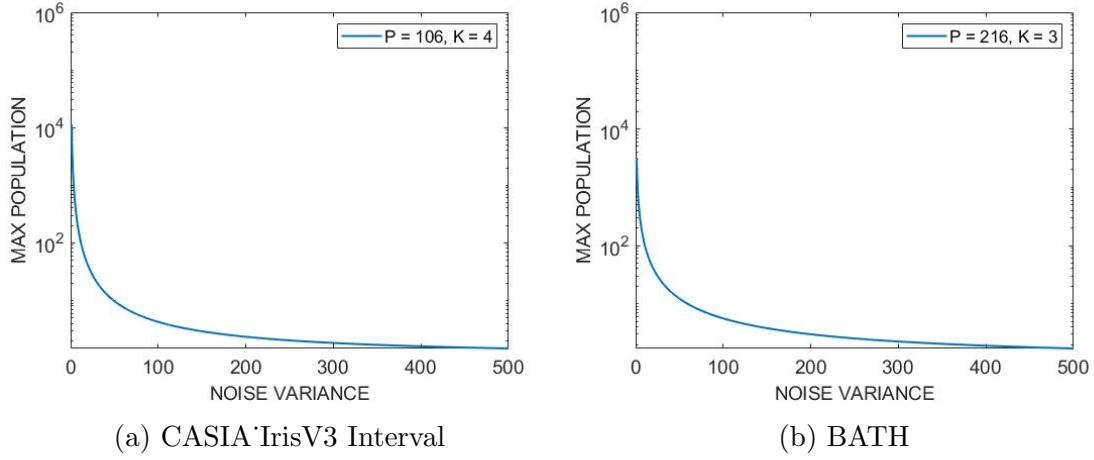


Figure 3.24: Sphere Packing Bound for (a) CASIA-IrisV3 Interval and (b) BATH using the log-likelihood metric.

supported by BATH is significantly higher than that of CASIA-IrisV3 Interval for the relative entropy fitted values. While increasing the noise present in the classes themselves, the capacity of the database decreases exponentially. Because of this decaying maximum population in relation to noise variance, we can directly correlate the maximum supported population of the database on the images quality (noise) present within the database itself. Because of this, the bound is also provide a measurement of image quality, as image quality decreases (noise variance increases) the maximum population attainable also decreases at a rapid rate.

This bound is also very sensitive on the one-to-one mapping of the iris images themselves, which is demonstrated in the likelihood bounds for both databases. Since the best-fitted degrees of freedom, K , for the BATH database is one degree lower than the CASIA-IrisV3 Interval database, the maximum population is lower by a power of ten. Fundamentally this makes sense, as the length of the Gaussian codeword in which each iris is mapped is dependent on the degrees of freedom fitted from the relative frequencies of each distance metric. Although this bound is not perfect, it still gives researchers an attainable bound to analyze their iris databases.

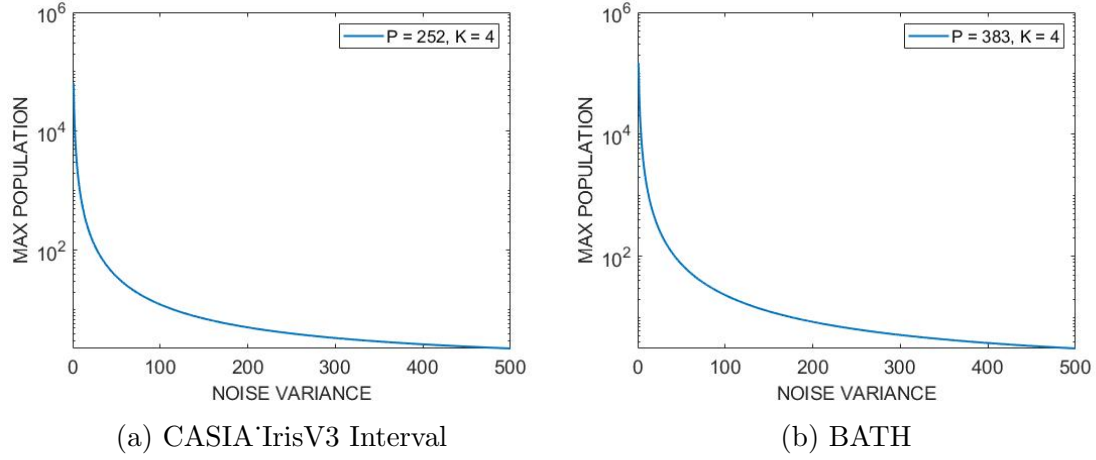


Figure 3.25: Sphere Packing Bound for (a) CASIA-IrisV3 Interval and (b) BATH using the relative entropy metric.

Table 3.3: Select Sphere Packing Bound Values based on Noise Variance (N) from Figure 3.24 and Figure 3.25.

<i>Noise Variance</i> (N)	Relative Entropy		Likelihoods	
	M_{CASIA}	M_{BATH}	M_{CASIA}	M_{BATH}
1	6.40×10^4	1.48×10^5	1.15×10^4	3.2×10^3
10	686	1.54×10^3	134	107
50	36	74	9	12
100	12	23	4	5
200	5	8	2	2
300	3	5	2	2
400	2	3	2	2
500	2	3	2	2

3.6 Daugman-like Bound

Once again using the best-of-fit chi-square distributions from Section 3.4, the maximum population of both databases can be evaluated through the use of our developed Daugman-like bound given in equation 3.21. The maximum population, M , is dependent on a fixed recognition error of the system, δ , and the false match rate (FMR) given a certain relative entropy threshold, T . Similar to Daugman [17], the

fixed recognition errors are varied at 50%, 10%, 1%, and .1%. To find the FMR, the cumulatives of the fitted chi-square distribution ($\chi_K^2(T)$) for each database, from equation 3.23, are obtained given the relative entropy values from Figure 3.22. Figure 3.26 shows the resulting bound for CASIA-IrisV3 Interval and BATH databases given varying fixed recognition errors. Table 3.4 displays a subset of the maximum population for each recognition error with increasing relative entropy.

Looking at Table 3.4, the most desirable case would be with a relative entropy of $T = 1$ and a recognition error of $\delta = 0.001$, where we have very clean (no noise) data and our recognition error for the system is extremely low. From this singular case, we can see that the maximum supported population for CASIA-IrisV3 Interval is $M = 2.43 \times 10^7$ and for BATH is $M = 1.30 \times 10^8$. These results follow with our observations of the Sphere-Packing bound population, in Section 3.5, where the BATH database is able to sustain more classes than CASIA-IrisV3 Interval (approx. 20% more capacity) due to its high image quality. This bound also shows the dependance of image quality on maximum population and as the relative entropy between two p.d.f.s of the iris models increases, the maximum population of classes for the database decreases exponentially. While this low relative entropy seems unattainable, due to current developments in modern cameras and imaging techniques, a low threshold is feasible by ensuring that enrollment and authentication data is of the highest quality using these modern devices.

4.0 Summary

This chapter introduces a new methodology for finding the capacity of an iris database utilizing its raw data. This methodology leverages two derived distance metrics, an asymptotic log-likelihood test and the relative entropy between classes'

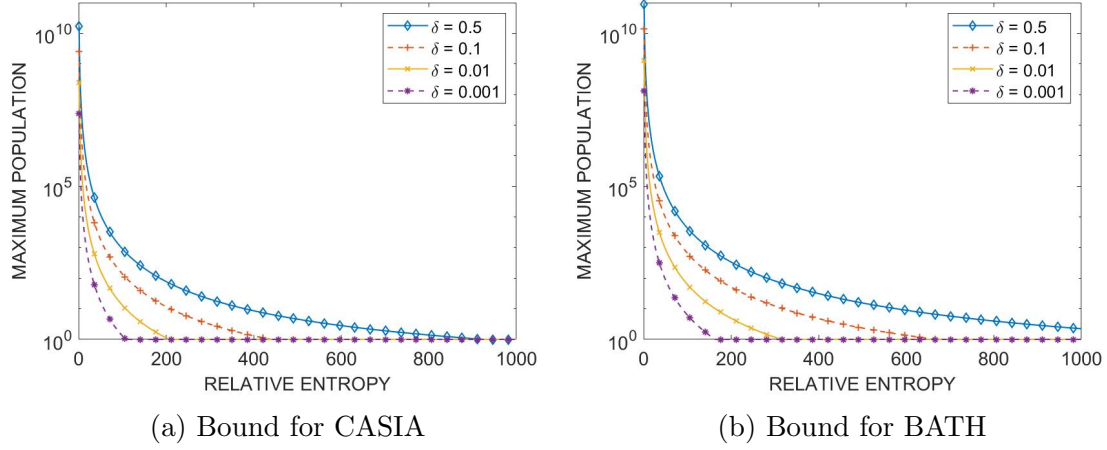


Figure 3.26: Daugman-like Bound for (a) CASIA and (b) BATH datasets.

Table 3.4: Subset of Daugman-like bound maximum population values with fixed recognition errors (δ) and varying relative entropy metric (T).

T	$\delta = 0.5$		$\delta = 0.1$		$\delta = 0.01$		$\delta = 0.001$	
	M_{CASIA}	M_{BATH}	M_{CASIA}	M_{BATH}	M_{CASIA}	M_{BATH}	M_{CASIA}	M_{BATH}
1	1.68×10^{10}	8.97×10^{10}	2.56×10^9	1.36×10^{10}	2.44×10^8	1.33×10^9	2.43×10^7	1.30×10^8
10	5.73×10^6	3.02×10^7	8.71×10^5	4.50×10^6	8.31×10^4	4.38×10^5	8.27×10^3	4.36×10^4
50	1.21×10^4	6.12×10^4	1.84×10^3	2.30×10^3	175	886	17	88
100	902	4.32×10^3	137	657	13	62	2	6
200	77	335	11	50	2	4	2	2
400	8	31	2	4	2	2	2	2
600	2	8	2	2	2	2	2	2
800	2	3	2	2	2	2	2	2
1000	2	2	2	2	2	2	2	2

estimated power spectral densities using an Auto-regressive model. Once the distance between each combination of classes is found, the relative frequencies (histograms) are fitted with chi-square distributions to establish a one-to-one mapping utilizing their fitted degrees of freedom and variance. This mapping to a unique Gaussian codeword for each class allows for the derivation of a Gaussian Sphere-Packing bound and a Daugman-like bound to evaluate an iris database's capacity and measure image quality.

From the bounds presented in Section 3.5 and 3.6, we conclude that the maximum population is dependent on the image quality present in each database. This is proved through the observation that the BATH database has a higher capacity than the CASIA-IrisV3 Interval due to the higher quality of images present. With more advanced acquisition techniques and state-of-the art signal processing techniques to improving data quality, the upper bounds presented are feasible for researchers. In conclusion, this proposed methodology allows researchers to find the sustainable maximum population of their iris database and measure their image quality.

Chapter 4

Proposed Future Work

While this thesis presents two new methodologies to find iris uniqueness, there are additional investigations to be performed within the work itself and future explorations for an extension of this work. This section provides ideas for future work for researchers motivated to continue measuring biometric uniqueness.

Implementation of a one-to-one mapping: The next direction of future work would be to implement a one-to-one mapping in both Chapters 2 and 3. In both works, we represent a single iris based on the fitted imposter distributions degrees-of-freedom; however, we do not implement this step practically to find the actual supported maximum population. To achieve this, new and classical channel encoding techniques, such as auto-encoders or a neural network, should be explored and implemented in our methodologies.

Types of vectorization: In the second methodology presented, in Chapter 3, we implemented a ZigZag vectorization to unwrap our iris data from 2D to 1D vector. We also analyzed the effects that traditional row-by-row vectorization had on performance in Section 3.3.3. Because only two types of vectorization were explored, other methods should be analyzed and the performance of measuring uniqueness should be evaluated.

Looking at different codes: While Chapter 2 focuses on Daugman’s encoding technique to generate his IrisCode, the research of different encoding techniques used in practice today was not explored. Other encoding algorithms are likely to produce a different number of degrees of freedom. Because of this, the theory presented in Chapter 2 can be applied to current iris encoding techniques.

Looking at measuring uniqueness of different biometrics: The methodology presented in Chapter3 may apply to different biometrics, such as the face, fingerprint, palm print, etc. Because of this, the procedure presented in Chapter 3 can be implemented on different databases. When measuring the uniqueness of different biometrics, the extension would be to combine the biometric modalities that provide the most unique information for each subject and use these modalities in a multi-modal biometric recognition system.

Extension into security: Since the motivator for measuring the uniqueness of a biometric is security-related, this provides a natural extension into biometric security. All the future work ideas presented above have security implications. For example, when providing a one-to-one encoding for each iris, we can also include encryption, such that each person has their unique identifier, and use this newly developed code for identification.

Appendix A

Related Publications

Jinyu Zuo, Katelyn M. Hampel, and Natalia A. Schmid. “New Perspectives on Recognition Performance of Daugman’s IrisCode or “Everything is New—it is Well Forgotten Old””. In: *IEEE Access* 9 (2021), pp. 158632–158637. doi: 10.1109/ACCESS.2021.3130100.

References

- [1] A. Adler, R. Youmaran, and S. Loyka. “Towards a measure of biometric information”. In: *2006 Canadian conference on electrical and computer engineering*. IEEE. 2006, pp. 210–213.
- [2] F. H. Adler. *Physiology of the Eye*. St. Louis, MO: Mosby, 1965.
- [3] H. Akaike. “A new look at the statistical model identification”. In: *IEEE Transactions on Automatic Control* 19.6 (1974), pp. 716–723. DOI: 10.1109/TAC.1974.1100705.
- [4] S. Ao, W. Ren, and S. Tang. “Analysis and Reflection on the Security of Biometric System”. In: *2008 4th International Conference on Wireless Communications, Networking and Mobile Computing*. 2008, pp. 1–5. DOI: 10.1109/WiCom.2008.2825.
- [5] L. A. Bassalygo. “New Upper Bounds for Error Correcting Codes”. In: *Problems of Information Transmission* 1 (4 1965), pp. 32–35. DOI: doi:10.1109/TIT.1960.1057584. URL: <http://mi.mathnet.ru/ppi762>.
- [6] R. M. Bolle et al. “Iris individuality: A partial iris model”. In: *Proceedings of the 17th International Conference on Pattern Recognition, 2004. ICPR 2004*. Vol. 2. IEEE. 2004, pp. 927–930.

- [7] G. Boole. *The Mathematical Analysis of Logic, being a Essay towards a Calculus of Deductive Reasoning*. London: George Bell: Cambridge: Macmillan, Barclay, and Macmillan, 1847.
- [8] K. W. Bowyer and M. J. Burge. *Handbook of Iris Recognition (Advances in Computer Vision and Pattern Recognition)*. New York: Springer, 2016.
- [9] J. P. Burg. “Maximum entropy spectral analysis”. PhD thesis. Department of Geophysics, Stanford University, Stanford, CA, 1975.
- [10] *CASIA Iris Image Database*. <http://biometrics.idealtest.org/>.
- [11] T. M. Cover and J. A. Thomas. *Elements of Information Theory*. Hoboken, NJ: Wiley-Interscience, 2006.
- [12] J. Daugman. “Biometric Personal Identification System Based on Iris Analysis”. US. Patent No. 5, 291,560. 1994.
- [13] J. Daugman. “Collision Avoidance on National and Global Scales: Understanding and Using Big Biometric Entropy”. In: *TechRxiv* (24-Feb-2021). DOI: 10.36227/techrxiv.14061671.v1.
- [14] J. Daugman. “How Iris Recognition Works”. In: *IEEE Transactions on Circuits and Systems for Video Technology* 14.1 (Jan. 2004), pp. 21–30.
- [15] J. Daugman. “Information Theory and the IrisCode”. In: *IEEE Transactions on Information Forensics and Security* 11.2 (2016), pp. 400–409. DOI: 10.1109/TIFS.2015.2500196. URL: <https://doi.org/10.1109/TIFS.2015.2500196>.
- [16] J. Daugman. “Probing the uniqueness and randomness of iriscodes: Results from 200 billion iris pair comparisons”. In: *Proceedings of the IEEE* 94.11 (2006), pp. 1927–1935.

- [17] J. Daugman. “The importance of being random: statistical principles of iris recognition”. In: *Pattern Recognition* 36 (2003), pp. 279–291.
- [18] B. Ergen. “Scale invariant and fixed-length feature extraction by integrating discrete cosine transform and autoregressive signal modeling for palmprint identification”. In: *Turkish Journal of Electrical Engineering Computer Sciences* 24 (Jan. 2016), pp. 1768–1781. DOI: 10.3906/elk-1309-65.
- [19] E. N. Gilbert. “A comparison of signalling alphabets”. In: *Bell System Technical Journal* 31 (1952), pp. 504–522. DOI: 10.1002/j.1538-7305.1952.tb01393.x.
- [20] R. C. Gonzalez and R. E. Woods. *Digital Image Processing*. Upper Saddle River, NJ: Pearson Education, Inc., 2008.
- [21] F. Gray. “Pulse Code Communication”. US. Patent 2,632,058. Serial No. 785697. 1953.
- [22] P. Grother et al. *IREX III - Performance of Iris Identification Algorithms*. en. 2012-04-03 2012. DOI: <https://doi.org/10.6028/NIST.IR.7836>.
- [23] S. M. Kay. *Fundamentals of Statistical Signal Processing. Volume II: Detection Theory*. New Jersey: Prentice Hall, 1998.
- [24] J. H. van Lint. *Introduction to Coding Theory*. Berlin: Springer-Verlag, 1999.
- [25] L. Masek and P. Kovesi. *MATLAB Source Code for a Biometric Identification System Based on Iris Patterns*. 2003. URL: <https://www.peterkovesi.com/studentprojects/libor/sourcecode.html>.
- [26] D. M. Monro, S. Rakshit, and D. Zhang. “DCT-Based Iris Recognition”. In: *IEEE Transactions on Pattern Analysis and Machine Intelligence* 29.4 (2007), pp. 586–595. DOI: 10.1109/TPAMI.2007.1002.

- [27] M. Plotkin. “Binary codes with specified minimum distance”. In: *IRE Transactions on Information Theory* 6 (1960), pp. 445–450. DOI: doi:10.1109/TIT.1960.1057584.
- [28] C. Rathgeb and C. Busch. *Iris and Periocular Biometric Recognition (Security)*. Stevenage, UK: The Institution of Engineering and Technology, 2017.
- [29] R. M. Ross. *Introduction to Coding Theory*. New York: Cambridge, 2007.
- [30] N. A. Schmid and F. Nicolo. “On empirical recognition capacity of biometric systems under global PCA and ICA encoding”. In: *IEEE Transactions on Information Forensics and Security* 3.3 (2008), pp. 512–528.
- [31] R. H. Shumway and D. S. Stoffer. *Time Series Analysis and Its Applications: With R Examples*. New York: Springer, 2017.
- [32] P. Stoica and Y. Selen. “Model-order selection: a review of information criterion rules”. In: *IEEE Signal Processing Magazine* 21.4 (2004), pp. 36–47. DOI: 10.1109/MSP.2004.1311138.
- [33] E. Tabassi, P. Grother, and W. Salamon. *IREX II - IQCE Iris Quality Calibration and Evaluation Performance of Iris Image Quality Assessment Algorithms*. en. 2011. URL: <https://www.nist.gov/itl/iad/image-group/irex-ii-iqce>.
- [34] J. H. Van Lint. “A Survey of Perfect Codes”. In: *The Rocky Mountain Journal of Mathematics* 5.2 (1975), pp. 199–224. URL: <https://www.jstor.org/stable/44236426>.
- [35] H. L. Van Trees. *Detection, Estimation and Modulation Theory: Part 1*. New York: John Wiley & Sons, Inc., 2001.

- [36] R. R. Varshamov. “Estimate of the number of signals in error correcting codes”. In: *Dokl. Akad. Nauk SSSR* 117 (1957), pp. 739–741.
- [37] Y. L. Wang et al. “Fingerprint compression: An adaptive and fast DCT-based approach”. In: *2010 IEEE International Conference on Image Processing*. 2010, pp. 3109–3112. DOI: 10.1109/ICIP.2010.5654009.
- [38] R. P. Wildes. “Iris recognition: an emerging biometric technology”. In: *Proceedings of the IEEE* 85.9 (1997), pp. 1348–1363. DOI: 10.1109/5.628669.
- [39] S. Yoon et al. “On the individuality of the iris biometric”. In: *International Conference Image Analysis and Recognition*. Springer. 2005, pp. 1118–1124.
- [40] J. Zuo, K. M. Hampel, and N. A. Schmid. “New Perspectives on Recognition Performance of Daugman’s IrisCode or “Everything is New—it is Well Forgotten Old””. In: *IEEE Access* 9 (2021), pp. 158632–158637. DOI: 10.1109/ACCESS.2021.3130100.